



Available online at www.sciencedirect.com

ScienceDirect

Geochimica et Cosmochimica Acta 143 (2014) 207–231

**Geochimica et
Cosmochimica
Acta**

www.elsevier.com/locate/gca

Postcollisional potassic and ultrapotassic rocks in southern Tibet: Mantle and crustal origins in response to India–Asia collision and convergence

Dong Liu^a, Zhdan Zhao^{a,*}, Di-Cheng Zhu^a, Yaoling Niu^{a,b,c},
Donald J. DePaolo^d, T. Mark Harrison^e, Xuanxue Mo^a, Guochen Dong^a,
Su Zhou^a, Chenguang Sun^f, Zhaochong Zhang^a, Junlai Liu^a

^a State Key Laboratory of Geological Processes and Mineral Resources, and School of Earth Science and Resources, China University of Geosciences, Beijing 100083, China

^b Institute of Oceanology, Chinese Academy of Sciences, Qingdao 266071, China

^c Department of Earth Sciences, Durham University, Durham DH1 3LE, UK

^d Center for Isotope Geochemistry, University of California, Berkeley, CA 94720, USA

^e Department of Earth and Space Sciences, University of California, Los Angeles, CA 90095-1567, USA

^f Department of Geological Sciences, Brown University, Providence, RI 02912, USA

Available online 8 April 2014

Abstract

Postcollisional potassium-rich magmatism in southern Tibet provides an important insight into the deep processes inducing accelerated plateau uplift and associated geologic episodes during early Miocene. As a major outcropping of postcollisional magmatic rocks in the southwestern Tibet, ultrapotassic and potassic volcanism in Xungba basin occurred coevally at ~23 Ma, consisting of bimodal-like volcanic sequence. The mantle-derived ultrapotassic rocks (Group 1) are latites and marked by both mantle and crustal geochemical signatures, similar to other younger (19–10 Ma) ultrapotassic rocks elsewhere in the southern Tibet. The high Th/Yb ratios, low Ba/La and Hf/Sr ratios observed in ultrapotassic rocks strongly imply derivation from a metasomatized lithospheric mantle regions enriched by inputs of pelagic sediment and carbonate during previous Tethyan oceanic subduction, while their relatively high SiO₂ and Dy/Yb, low Ni/MgO and CaO/Al₂O₃, and convex upward ⁸⁷Sr/⁸⁶Sr–δ¹⁸O_{V-SMOW} relationship suggest additional contributions of overthickened lower crust and ancient basement except for enriched mantle sources. The potassic rocks (Group 2), which underlie Group 1 rocks, are intermediate to silicic and exhibit adakitic geochemical affinities with high Sr/Y and La/Yb ratios, and low Y and Yb concentrations. The fingerprint of overthickened lower crust identified both from ultrapotassic and potassic rocks may be an important feature for magmatism occurred under the background of continental collision. And the bimodal volcanic sequence of Xungba post-collisional magmatism may further corroborate that the removal of lower part of over-thickened lithospheric mantle at depth have triggered an extension setting associated with Miocene plateau uplift.

© 2014 Elsevier Ltd. All rights reserved.

1. INTRODUCTION

* Corresponding author at: State Key Laboratory of Geological Processes and Mineral Resources, China University of Geosciences, 29 Xueyuan Road, Haidian District, Beijing 100083, China.
Tel./fax: +86 10 8232 1115; +86 1368 111 8299 (mobile).

E-mail address: zdzhao@cugb.edu.cn (Z. Zhao).

Following the closure of the Neo-Tethys ocean in the early-Paleogene (Mo et al., 2007, 2008; Royden et al., 2008; Lee et al., 2009; Bouilhol et al., 2013), continued convergence of India–Asia has lead to large-scale mantle–crust

interactions that may have been responsible for a variety of geological phenomena and the uplift of Tibetan Plateau in the Miocene (DePaolo and Ingram, 1985; Harrison et al., 1992; Yin and Harrison, 2000; Guo et al., 2008; Kapp et al., 2008; Molnar and Stock, 2009; Enkelmann et al., 2011; Kirstein, 2011). The postcollisional magmatism such as the late Oligocene–Miocene adakitic rocks of deep crustal origin and the ultrapotassic rocks of mantle origin offer unprecedented opportunities to reveal deep processes (e.g., deep subduction of Indian continental materials, convective thinning of the lithosphere, and delamination of overthickened lower crust) associated with the India–Asia continental collision and continued convergence (Miller et al., 1999; Ding et al., 2003; Nomade et al., 2004; Williams et al., 2004; Chung et al., 2005; Zhao et al., 2009; Guo et al., 2013; Liu et al., 2014). An important observation concerns the geochemical signatures of continental crust displayed by mantle-derived ultrapotassic rocks. Such signatures have long been interpreted as resulting from mantle sources enriched by deep processes, including mantle metasomatism by oceanic sediments and/or Indian continental crust (Miller et al., 1999; Ding et al., 2003; Williams et al., 2004; Zhao et al., 2009; Guo et al., 2013), which then led to the tectonic interpretation that the ultrapotassic magmatism marks the removal and melting of southern Tibet continental mantle lithosphere with metasomatic histories.

However, whether the metasomatic agents are subducted seafloor sediments and/or Indian crustal material remains in dispute (Williams et al., 2004; Gao et al., 2007; Zhao et al., 2009; Tommasini et al., 2010; Guo et al., 2013). In the Lhasa terrane, the Mesozoic-early Cenozoic magmatism resulting from the Tethyan seafloor subduction would have led to the Tibetan mantle lithosphere metasomatized with either or both of the aforementioned agents before India–Asian continental collision (DeBon et al., 1986; Dewey et al., 1988; Chung et al., 2005; Chu et al., 2006; Gao et al., 2007; Ji et al., 2009; Tommasini et al., 2010; Zhu et al., 2011a, 2013; Liu et al., 2014). Geophysical studies show that the north-dipping Indian lithosphere has reached the the Bangong-Nujiang suture zone at depth (Kosarev et al., 1999; Nábělek et al., 2009), which supports the scenario of Indian crust material as a possible metasomatic agent (Zhao et al., 2009; Liu et al., 2011a; Guo et al., 2013). Importantly, recent studies have found crustal xenoliths and a variety of zircon xenocrysts with pre-eruptive U–Pb ages in the ultrapotassic rocks (Sun et al., 2008; Hébert et al., 2014; Liu et al., 2013, 2014), providing evidence for the Lhasa terrane crust contributions to the Tibetan ultrapotassic magmatism. Previous studies proposed that an over-thickened crust may have formed as a result of continuous continental convergence (Chung et al., 2005, 2009) and the mature Precambrian basement of the central Lhasa subterrane shares similar isotopic composition to that of the Indian crust (Zhu et al., 2011b, 2012a; Zhang et al., 2012). All these observations point to the significance of the Lhasa terrane crustal material (i.e., in addition to Tethyan seafloor sediments and underthrust Indian basement) in the petrogenesis of the postcollisional potassio–ultrapotassic magmatism in southern Tibet.

In this paper, we present the results of our comprehensive study of postcollisional magmatism from the Xungba Basin (Fig. 1), which forms a “bimodal” volcanic sequence composed of early-Miocene ultrapotassic lavas and the underlying potassio lavas with adakitic geochemical signature (Liu et al., 2011b). The results include high quality zircon U–Pb age data and Hf isotopes, whole rock major and trace element compositions, and Sr–Nd–Pb–O isotopes. These data allow us to (i) clarify the relationship between ultrapotassic and adakitic magmatism and their constraints on the onset of the regional extension, (ii) place the timing on the lithospheric thinning/delamination in the Lhasa terrane, and (iii) probe the nature of the overthickened southern Tibetan lithosphere. Built on the previous studies, this study highlights the significance of crustal contributions (thickened lower crust and ancient Lhasa basement) in the petrogenesis of the Tibetan postcollisional magmatism, and provides enhanced understanding of crustal control on postcollisional magmatism in the context of India–Asia convergence.

2. GEOLOGICAL BACKGROUND

The Lhasa terrane, bounded by the Indus-Yarlung Zangbo suture zone (IYZS) in the south and the Bangong-Nujiang suture zone (BNS) to the north, was subjected to northward Neo-Tethyan seafloor subduction prior to the India–Asia continental collision and postcollisional underthrusting of the Indian continent (Owens and Zandt, 1997; Yin and Harrison, 2000). Recent studies suggest that the Lhasa terrane can be divided into three sub-units (the northern, central, and southern Lhasa subterrane), separated by the Shiquanhe-Nam Tso mélange zone (SNMZ) and Luobadui-Milashan fault (LMF), respectively (Zhu et al., 2011a, 2013) (Fig. 1a). These three units have significantly different sedimentary, magmatic and tectonic histories and appear to have distinctive crustal compositions.

In the northern Lhasa subterrane, the oldest sequences are middle Triassic sedimentary strata interbedded with volcanic rocks (Zhu et al., 2013). The Cretaceous magmatism, including the Duoni formation volcano-sedimentary strata (ca. 116–91 Ma; Kang et al., 2008) and Baingoin batholith (ca. 132–113 Ma; Zhu et al., 2013), is widely distributed in the northern Lhasa subterrane and is interpreted to have resulted from southward subduction of the Bangong-Nujiang Tethyan seafloor and continental collision thereafter (Zhu et al., 2011a, 2013). In the southern Lhasa subterrane, the Mesozoic sedimentary cover is restricted to the eastern portion and separated from the passive continental margin sedimentary sequence in the Tethyan Himalaya by the IYZS (Zhu et al., 2013). The widespread Gangdese Batholith and syncollisional Linzizong volcanic succession are regarded as the product of northward subduction and subsequent break-off of the Yarlung Zangbo Tethyan oceanic slab (Coulon et al., 1986; Chung et al., 2005; Mo et al., 2007, 2008; Ji et al., 2009; Lee et al., 2009; Zhao et al., 2011; Niu et al., 2013). The Mesozoic–Cenozoic granitoid magmatism in both the northern and southern Lhasa subterrane is characterized by high zircon $\varepsilon_{\text{Hf}}(t)$ values, low radiogenic Sr isotope and unradiogenic

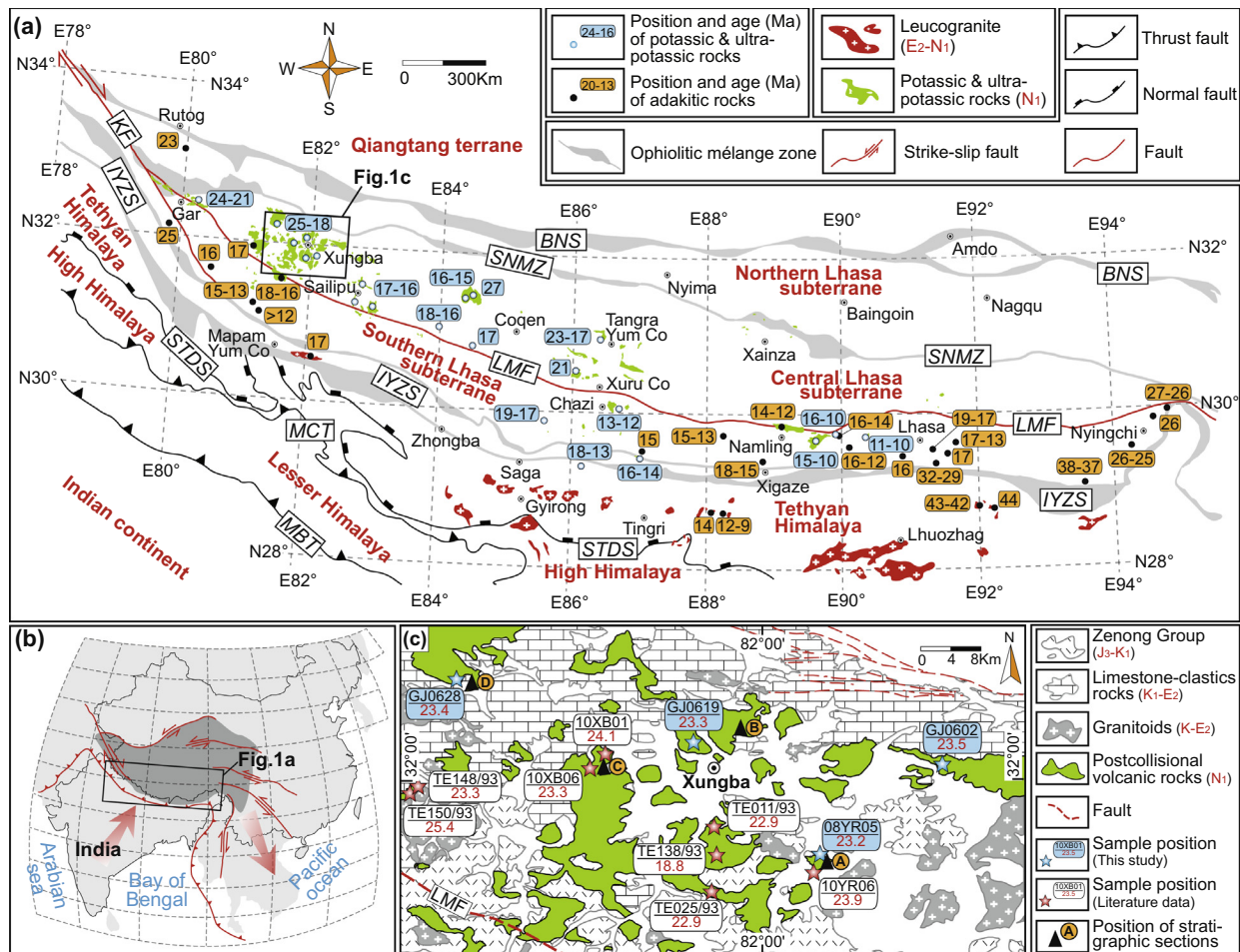


Fig. 1. (a) Simplified geological map of southern Tibet showing the main tectonic units (Lee et al., 2009; Zhu et al., 2011b) and spatial and temporal distribution of postcollisional magmatic rocks. (b) Simplified map showing tectonic outline of the Tibetan Plateau with main fault zones related to continental extrusion (Harrison et al., 1992). (c) Simplified geological map showing outcrops of postcollisional volcanic rocks and localities where volcanic rocks are dated in the Xungba basin (Miller et al., 1999; Liu et al., 2011b). Major outcrops of postcollisional potassic–ultrapotassic rocks in the central Lhasa subterrane include Shiquanhe (24–21 Ma; Williams et al., 2004), Xungba-Bangba-Yare (25–18 Ma; Miller et al., 1999; Chen et al., 2011; Liu et al., 2011b), Sailipu (17–16 Ma; Sun et al., 2008), Zabuye-Bugasi (27–15 Ma; Nomade et al., 2004), Maiga-Gongmutang (18–16 Ma; Ding et al., 2006; Zhao et al., 2009), Tangra Yum Co-KonglongXiang (23–17 Ma; Ding et al., 2003; Chen et al., 2010), and Xuru Co (13–12 Ma; Ding et al., 2003; Zhao et al., 2006). Potassic–ultrapotassic rocks in the southern Lhasa subterrane include Daggyai Tso-Pabbai Zong (19–13 Ma; Williams et al., 2001, 2004), Xuena-Xigaze (18–14 Ma; Chan et al., 2009; Liu et al., 2013), Namling-Wuyu (15–10 Ma; Zhao et al., 2001; Spicer et al., 2003; Williams et al., 2004), Majiang (16–10 Ma; Coulon et al., 1986), and Yangying (11–10 Ma; Nomade et al., 2004). Data of adakitic rocks and leucogranite in the southern Lhasa subterrane and Tethyan Himalaya are from Guo et al. (2007), Chung et al. (2009), Zeng et al. (2011), Chen et al. (2011), Guan et al. (2012), Guo and Wilson (2012), and Hou et al. (2012). BNS = Bangong-Nujiang suture zone; SNMZ = Shiquan river-Nam Tso mélange zone; LMF = Luobadui-Milashan fault; KF = Karakorum fault; IYZS = Indus-Yarlung Zangbo suture zone.

Nd isotope ratios largely due to the mantle input (Chung et al., 2009; Ji et al., 2009; Wu et al., 2010; Chu et al., 2011; Zhu et al., 2011a).

In contrast, the central Lhasa subterrane underlain by Archean to Proterozoic basement may represent a fragment of a micro-continent separated from east Gondwana that drifted across the Tethyan Ocean (Zhu et al., 2011b; Zhang et al., 2012). Although the outcrops of the Precambrian basement have only been identified in the eastern part of the central Lhasa subterrane to date (Nyainqntanglha Group, 780–690 Ma; Kapp et al., 2005; Dong et al.,

2010), inherited Precambrian zircons have been identified in Mesozoic magmatic rocks from the western part of the central Lhasa subterrane (Zhu et al., 2011a, 2013). The sedimentary sequences in the central Lhasa subterrane, ranging from Ordovician to the early Mesozoic, are mainly composed of fine-grained marine clastic and carbonate rocks (Yin and Harrison, 2000). Late Jurassic to early Cretaceous volcano-sedimentary rocks of the Zenong formation, as well as age-equivalent granitoids, are abundant throughout the central Lhasa subterrane and have also been attributed to the subduction and slab break-off of the Bangong-Nujiang

oceanic lithosphere (Kang et al., 2008; Zhu et al., 2011a, 2013). Besides, the contribution from ancient basement to the Mesozoic–Cenozoic magmatism in the central Lhasa subterrane is evident because of the enriched Sr–Nd–Hf isotopic compositions (Zhao et al., 2011; Zhu et al., 2011a; Lee et al., 2012).

The postcollisional magmatism in the Lhasa terrane, including potassic-ultrapotassic volcanic rocks, adakitic intrusives, and minor leucogranite, is distributed roughly parallel to the sutures along the Lhasa terrane and Himalayan orogenic belt (Chung et al., 2005; Zhao et al., 2009) (Fig. 1a) and is spatially related to the N–S trending extensional faults (cf. Coulon et al., 1986; Zhao et al., 2006). The postcollisional magmatism in the central Lhasa subterrane extends to Shiquanhe to the west and Tangra Yum Co to the east, which consists of potassic volcanic rocks (PVR) and ultrapotassic volcanic rocks (UPVR). These potassium-rich rocks, with eruptive ages ranging from 27 to 12 Ma, show extremely high Sr but low Nd isotopic ratios (Miller et al., 1999; Ding et al., 2003; Williams et al., 2004; Zhao et al., 2006, 2009; Gao et al., 2007, 2009; Chen et al., 2010, 2012; Guo et al., 2013).

In the southern Lhasa subterrane, the postcollisional magmatism is dominated by adakitic intrusive rocks and minor PVR–UPVR that occurred as veins, volcanic and sub-volcanic rocks of 20–10 Ma age with a juvenile crustal signature (Coulon et al., 1986; Williams et al., 2001; Zhao et al., 2001; Hou et al., 2004; Chung et al., 2005, 2009). In the Himalayan orogenic belt, Miocene leucogranites formed by crustal anatexis display isotopic compositions that may represent subducted Indian basement (Harrison et al., 1997; Zeng et al., 2011; Guo and Wilson, 2012; Hou et al., 2012). Near the eastern syntaxis, Eocene–Oligocene high Sr/Y rocks have been identified in the southern Lhasa subterrane (26–38 Ma; Harrison et al., 2000; Hou et al., 2004; Guo et al., 2007; Chung et al., 2009; Guan et al., 2012) and the Tethyan Himalaya (43–44 Ma; Aikman et al., 2008, 2012; Zeng et al., 2011; Hou et al., 2012).

3. LOCATION AND PETROGRAPHY OF SAMPLES

The Xungba basin, situated in the northern part of the N–S trending Xungba–Yare rift, contains the largest known outcrops of postcollisional magmatic rocks in the central Lhasa subterrane (Fig. 1a). Folded Mesozoic strata, which mainly consist of marine facies sedimentary rocks interbedded within volcanic flows, cover the northern part of the basin. The subduction-related Zenong group volcano-sedimentary strata are restricted to the southern part of the basin (Fig. 1c). According to the composition and abundances of phenocrysts (brief description has been summarized in [Supplementary Online Material \(SOM\) Table 1](#)) and stratigraphic contact relationships (Fig. 2), the Xungba postcollisional volcanic rocks can be subdivided into ultrapotassic latite (Group 1; UPVR) and potassic intermediate-silicic rocks (Group 2; PVR).

The latitic upper portion (Group 1) of the Xungba lava flows is mainly found in southern Xungba basin, in clear unconformable contact with underlying carbonate strata

(Figs. 2 and 3a) and contains crustal xenoliths (Fig. 3b). They have porphyritic and synneusis textures (Fig. 3c) with 10–15 vol.% in phenocrysts (clinopyroxene, orthopyroxene, olivine, plagioclase, and phlogopite). Zoning and pervasive resorption textures are very common for pyroxenes from the UPVR (Fig. 3d and e), which exhibits irregular dark finely spongy cellular structure in the center (Fig. 3d) or coarsely cellular structure to the rim (Fig. 3e). In a latite sample, subhedral rutile xenocrysts were also found (Fig. 3g). Compared with the phenocrysts in latites (Group 1), the potassic intermediate-silicic rocks (Group 2), which occurred as the lower part of the Xungba lava flows (Fig. 2), contain more sanidine and plagioclase (Fig. 3h and i) with minor biotite, hornblende, and orthopyroxene.

In addition to the field superposition relationship between UPVR and PVR (lithostratigraphic columns C in Fig 2), their similar eruptive ages, which are consistent with previously published data (Table 1), further suggest that these postcollisional rocks formed as the result of the same tectono-magmatic event. The early-Miocene ages indicate that they are the earliest postcollisional magmatic rocks in southern Tibet (Fig. 1a) (cf. Chung et al., 2005; Zhao et al., 2006, 2009).

4. ANALYTICAL METHODS

4.1. Zircon U–Pb dating, trace element and Hf isotopes

Zircons were extracted from coarsely crushed samples (80 mesh). They were separated by using combined methods of heavy liquid and magnetic separation before hand-picking under a binocular. The selected zircons were mounted in epoxy resins and were polished to expose grain interiors. Cathodoluminescence (CL) images were obtained by using scanning electron microscope (SEM, Leo 1450VP, Germany) at the Institute of Geology and Geophysics, Chinese Academy of Sciences (IGG–CAS) before *in situ* U–Pb and Hf isotopes analyses.

Zircon U–Pb dating and trace element analysis were acquired simultaneously using LA-ICP-MS at the State Key Laboratory of Geological Processes and Mineral Resources (GPMR), China University of Geosciences, Wuhan. Laser sampling was performed using 193 nm excimer laser ablation system (GeoLas 2005), and ion intensities were acquired using ICP-MS (Agilent 7500a). The diameter of spot was ~32 μm. Zircon standard 91500 was used as external standard for U–Pb dating (Wiedenbeck et al., 1995), and every five sample analyses was followed by analysis of two 91500 zircon standards. Each analysis includes a background acquisition of 20–30 s (gas blank) and 50 s data acquisition on the sample. Trace element abundances were calibrated against USGS multiple-reference materials (BCR-2G and BIR-1G) using ²⁹Si as an internal standard (Liu et al., 2010). Off-line selection and integration of background and sample signals, time-dependent drifts for U–Th–Pb isotopic ratios correction, U–Pb dating and quantitative calibration for zircon trace element analyses were all performed by *ICPMSDataCal_ver8.0* (Liu et al., 2010). Detailed operating conditions for the

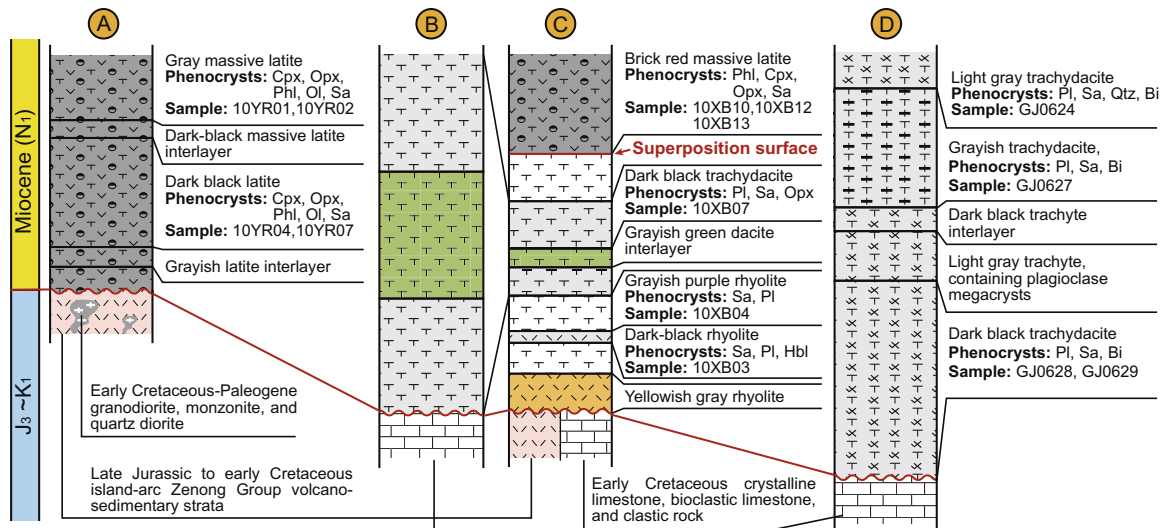


Fig. 2. Lithostratigraphic columns of Xungba postcollisional volcanic rocks. The locations of these columns are indicated in the Fig. 1c. Bi: biotite, Cpx: clinopyroxene, Hbl: hornblende, Ol: olivine, Opx: orthopyroxene, Phl: phlogopite, Pl: plagioclase, Qtz: quartz, and Sa: sanidine.

LA-ICP-MS and data reduction are the same as those described in Liu et al. (2008, 2010). Common lead correction procedure was based on Andersen (2002). Tera-Wasserburg diagrams and mean square of weighted deviates (MSWD) were calculated using *Isoplots/Ex_ver3* (Ludwig, 2003).

Zircon Hf isotopes were analyzed using a Nu Plasma HR MC-ICPMS (Nu Instruments Ltd., UK) coupled to a GeoLas 2005 excimer ArF laser-ablation system at the State Key Laboratory of Continental Dynamics, Northwest University (CDNU), Xi'an. The energy, pulse rate, and

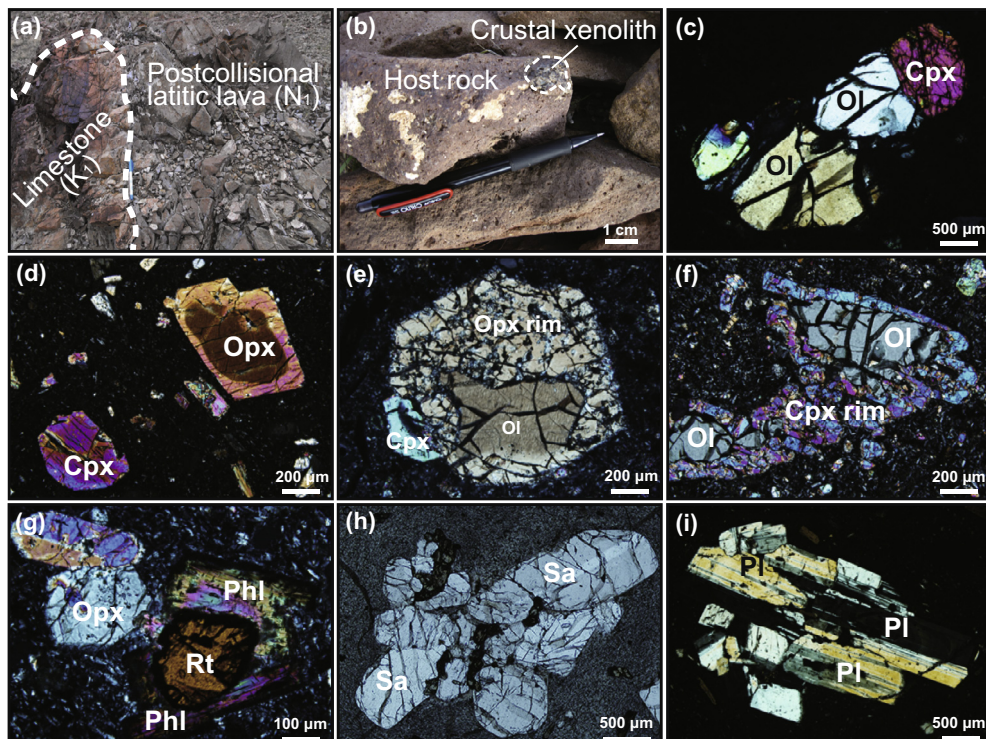


Fig. 3. (a) The unconformable contact between early-Miocene ultrapotassic rocks and underlying early Cretaceous limestone and clastic rocks. (b) Crustal xenolith entrained by ultrapotassic magma. (c) Phenocrystal clots composed of olivine with rounded or triangular shapes and subhedral clinopyroxene in the UPVR (Group 1). (d) Subhedral orthopyroxene and clinopyroxene phenocrysts of ultrapotassiac latite (Group 1). (e and f) Poikilitic olivine textures in the UPVR (Group 1): (e) orthopyroxene with coarsely cellular texture as a rim of irregular-shaped olivine grain, and (f) elliptical olivine grains included in clinopyroxene. (g) Rutile xenocryst in the UPVR (Group 1). (h) Sanidine phenocrystal clots in the PVR (Group 2). (i) Plagioclase phenocrystal clots with polysynthetic twinning in the PVR (Group 2).

Table 1

Dating results of postcollisional volcanic rocks in the Xungba basin, southwestern Tibet.

Affinity	Sample No.	Location	Dating results			
			Mineral/Rock	Method	Age $\pm 2\sigma$ (Ma)	Data source
UPVR	TE011/93	~10 km South of Xungba	Phl ^{40}Ar - ^{39}Ar	Ar-Ar MS	22.9 \pm 0.4	Miller et al. (1999)
UPVR	TE138/93	~15 km South of Xungba	Phl ^{40}Ar - ^{39}Ar	Ar-Ar MS	18.8 \pm 0.5	Miller et al. (1999)
UPVR	10YR06	~20 km Southeast of Xungba	Zircon U-Pb	LA-ICP-MS	23.9 \pm 0.6	Liu et al. (2011a)
UPVR	08YR05	~25 km south of Xungba	Zircon U-Pb	LA-ICP-MS	23.0 \pm 0.4	Liu et al. (2013)
PVR	TE025/93	~25 km South of Xungba	WR ^{40}Ar - ^{39}Ar	Ar-Ar MS	22.9 \pm 0.2	Miller et al. (1999)
PVR	TE148/93	~25 km South of Bangba	WR ^{40}Ar - ^{39}Ar	Ar-Ar MS	23.3 \pm 0.2	Miller et al. (1999)
PVR	TE150/93	~25 km South of Bangba	WR ^{40}Ar - ^{39}Ar	Ar-Ar MS	25.4 \pm 0.2	Miller et al. (1999)
PVR	07BB03	~50 km South of Bangba	Zircon U-Pb	LA-ICP-MS	17.0 \pm 0.2	Chen et al. (2011)
PVR	10XB06	~15 km West of Xungba	Zircon U-Pb	LA-ICP-MS	23.3 \pm 0.4	Liu et al. (2011b)
PVR	GJ0602	~28 km East of Xungba	Zircon U-Pb	LA-ICP-MS	23.5 \pm 0.2	This study
PVR	GJ0619	~5 km Northwest of Xungba	Zircon U-Pb	LA-ICP-MS	23.3 \pm 0.2	This study
PVR	GJ0628	~15 km Southeast of Bangba	Zircon U-Pb	LA-ICP-MS	23.4 \pm 0.1	This study
PVR	10XB01	~15 km West of Xungba	Zircon U-Pb	LA-ICP-MS	24.1 \pm 0.3	Liu et al. (2011b)

UPVR, ultrapotassic volcanic rock; PVR, potassic volcanic rock.

spot size in this work were 100 mJ, 8 Hz, and 44 μm , respectively. High-purity helium was used as the carrier gas within the ablation cell and was mixed with argon (makeup gas) in the homogenizers. Each analysis includes 30 s data acquisition on the sample, and every ten-sample analysis was followed by one analysis of zircon standard 91500, GJ-1 and Monastery. Detailed operating conditions for MC-ICP-MS and the correction for interference by Lu and Yb have been described by Yuan et al. (2008). In this work, the average $^{176}\text{Hf}/^{177}\text{Hf}$ ratio for zircon standard 91500 was 0.282299 ± 15 (2σ , $n = 38$), which agrees well with the recommended value within error (Woodhead et al., 2004; Yuan et al., 2008).

4.2. Major and trace elements

For whole-rock geochemical analysis, well-cleaned fresh rock sample chips (dried at 50 °C) were crushed to 200 mesh after rejecting amygdale and xenoliths (crust and mantle) by hand-picking. Rock powders were mixed with 5.2 g $\text{Li}_2\text{B}_4\text{O}_7$ + 0.4 g LiF + 0.3 g NH_4NO_3 , and fused in a Pt crucible for major elements analysis using X-ray fluorescence spectrometry (XRF) at CDNU Xi'an. Trace element abundances were determined using ICP-MS (Agilent 7500a) at GPMR, Wuhan. Whole-rock powders (50 mg) for trace elements analysis were dissolved in Teflon bombs by HF + HNO₃, and the sealed Teflon bombs have been heated at 190 °C in oven for 48 h. After evaporating the solution in Teflon to incipient dryness at 115 °C, the resultant salt was re-dissolved by mixture of 30% HNO₃. The final solution was diluted to ~100 g with 2% HNO₃ in a polyethylene bottle. Detailed sample-preparing procedure, operating conditions for the laser ablation system and ICP-MS instrument, USGS rock reference materials (BCR-2, BHVO-2, AGV-2, RGM-1 and GSR-1) and data reduction have been described by Liu et al. (2008).

4.3. Whole-rock Sr–Nd–Pb–O isotopes

For whole-rock Sr–Nd isotope analysis, rock powders were dissolved in Teflon bombs using HF + HNO₃ +

HClO₄. Rb, Sr, Sm and Nd were separated by conventional ion exchange procedures and measured using a Finnigan MAT261 thermal ionization mass spectrometer (TIMS) in static mode at GPMR, Wuhan. The isotopic ratios were normalized to $^{86}\text{Sr}/^{88}\text{Sr} = 0.1194$ and $^{146}\text{Nd}/^{144}\text{Nd} = 0.7219$, respectively, for mass fractionation correction. Total procedural blanks are <1 ng for Sr and <50 pg for Nd. The Sr standard (NBS 607) and Nd standard (BCR-2) yielded $^{87}\text{Sr}/^{86}\text{Sr} = 0.710257 \pm 12$ (2σ) and $^{143}\text{Nd}/^{144}\text{Nd} = 0.512118 \pm 12$ (2σ), respectively. Detailed descriptions of the analytical procedures and operating conditions for TIMS are given in Liu et al. (2004). The $\varepsilon_{\text{Nd}}(t)$ was calculated with reference to CHUR $^{143}\text{Nd}/^{144}\text{Nd}$ ratios of 0.512638, and the neodymium isotopic depleted mantle model age (T_{DM}) was calculated by assuming its parental magma had been derived from depleted mantle source with $(^{147}\text{Sm}/^{144}\text{Nd})_{\text{DM}} = 0.21375$ and $(^{143}\text{Nd}/^{144}\text{Nd})_{\text{DM}} = 0.51315$. The decay constant of Nd is $6.54 \times 10^{-12} \text{ yr}^{-1}$.

For Pb isotopic analysis, rock powders (100–150 mg) were dissolved in Teflon bombs by purified HF + HNO₃ and were heated at 195 °C for 48 h. Separation of Pb was achieved by conventional ion exchange procedures and HCl was used as leaching agent. Pb isotopic ratios were determined using Nu Plasma HR MC-ICPMS at the CDNU, Xi'an and Thermo-Finnigan TRITON mass spectrometry equipped with an oxygen gas leak valve, nine Faraday cups and an ion counting multiplier at the Institute of Geology and Mineral Resources, Tianjin. In Xi'an, total procedural blanks were <20 pg. For mass fractionation correction, NBS 981 standards was analyzed in Xi'an with average values and associated errors (2σ) being $^{206}\text{Pb}/^{204}\text{Pb} = 16.942 \pm 0.002$, $^{207}\text{Pb}/^{204}\text{Pb} = 15.499 \pm 0.002$, and $^{208}\text{Pb}/^{204}\text{Pb} = 36.725 \pm 0.004$. In Tianjin, total procedural blanks were <1 ng, and NBS 982 standard was used to for mass fractionation. The average values of NBS 982 in this study were: $^{206}\text{Pb}/^{204}\text{Pb} = 36.624 \pm 0.002$, $^{207}\text{Pb}/^{204}\text{Pb} = 17.078 \pm 0.001$, and $^{208}\text{Pb}/^{204}\text{Pb} = 36.508 \pm 0.002$.

Oxygen isotopes were measured on a Finnigan MAT-253EM mass spectrometry at the Institute of Mineral

Resources, Chinese Academy of Geological Sciences. The mixture of purified BrF_5 and 9.5 mg sample powder was heated at 700 °C for 9 h under high vacuum condition. For oxygen isotopic analysis, the resultant oxygen was converted to CO_2 by reacting with graphite resistance rod for 12 min. Every five sample analysis was followed by one analysis of quartz standard NBS 28 ($\delta^{18}\text{O}_{\text{V-SMOW}} = 10.92\text{\textperthousand}$), and the analytical uncertainty is better than 0.2‰. All $\delta^{18}\text{O}$ values were reported with reference to the V-SMOW standard.

Zircon U-Pb age data, trace element (sample 08YR05) and Hf isotopic data are given in SOM Tables 2–4, respectively. Major and trace element data are given in Table 2, and whole-rock Sr-Nd-Pb-O isotopic compositions are given in Table 3.

5. RESULTS

5.1. Zircon morphology, trace elements and U-Pb geochronology

In CL images (Fig. 4), zircons from Group 1 UPVR samples (08YR05) are subrounded, and exhibit weak zoning, unzoned or uniform internal textures (Fig. 4a), which may imply a high-temperature crystallization environment (Corfu et al., 2003). In contrast to zircons from the PVR, zircons from the UPVR have relatively lower Th (94–468 ppm) and U (296–2420 ppm), with Th/U ratios >0.1 (Fig. 5a). Zircons from the UPVR can be subdivided into two types according to their different heavy rare earth element (HREE) patterns (Fig. 5b). The first type shows a rising slope from Ho to Lu [$(\text{Dy/Yb})_{\text{N}} = 0.20\text{--}0.43$] (Fig. 5b), together with homogeneous internal structure, consistent with magmatic zircons with mantle affinity (Belousova et al., 2002; Hoskin and Schaltegger, 2003), albeit with relatively higher U and Th concentrations (SOM Table S2). The second type is marked by generally flat HREE patterns [$(\text{Dy/Yb})_{\text{N}} = 0.81\text{--}1.34$] (Fig. 5b), which are similar to zircons crystallized under a very limited HREE supply (Rubatto, 2002; Liu et al., 2013, 2014). In spite of the divergence between two kinds of zircon, the U-Pb dating of UPVR zircons yield a weighted mean $^{206}\text{Pb}/^{238}\text{U}$ ages of 23.2 ± 0.4 Ma, after rejecting discordant ages (Fig. 4e).

Zircons from three PVR samples (GJ0602, GJ0619 and GJ0628) of Group 2 rocks commonly occur as doubly-terminated prismatic crystals, ranging from about 100 to 250 μm in size (Fig. 4b–d). Most zircons have narrow and frequent oscillatory zoning, and only a few of them show broad zoning. Except for a zircon grains (GJ0628-03) having extremely high Th concentration (19278 ppm) and relatively low Th/U ratios (0.23), most zircons in the PVR display higher Th (397–6151 ppm) and U (475–3737 ppm) concentrations than zircons in the UPVR (Fig. 5a). Their Th/U ratios (0.24–2.66) indicate a magmatic zircon origin (Hoskin and Schaltegger, 2003). After rejecting inherited zircon analytical spots, zircons from these PVR samples yield $^{206}\text{Pb}/^{238}\text{U}$ mean ages of 23.5 ± 0.2 , 23.3 ± 0.2 and 23.4 ± 0.1 Ma, respectively (Fig. 4f–h).

5.2. Zircon Hf isotopes

A total number of 58 dated zircons were analyzed by LA-MC-ICPMS for Hf isotope (SOM Table 4). Zircons from Group 1 UPVR sample (08YR05) exhibit highly variable $^{176}\text{Hf}/^{177}\text{Hf}$ ratios (0.282173–0.282686), $\varepsilon_{\text{Hf}}(t)$ values (−21.2 to −3.0) and depleted mantle model ages ($T_{\text{DM}} = 0.8\text{--}1.5$ Ga). By contrast, zircons in two PVR samples (GJ0602 and GJ0619) of Group 2 show relatively uniform Hf isotopic composition ($^{176}\text{Hf}/^{177}\text{Hf} = 0.282330\text{--}0.282427$), with $\varepsilon_{\text{Hf}}(t)$ and T_{DM}^{C} ranging from −15.6 to −12.2 and 1.9 to 2.1 Ga, respectively. Except for one analytical spot with most radiogenic Hf isotopic ratio ($^{176}\text{Hf}/^{177}\text{Hf} = 0.282531$, $\varepsilon_{\text{Hf}}(t) = -8.4$, $T_{\text{DM}}^{\text{C}} = 1.6$ Ga), most zircons in this PVR sample (GJ0628) have a narrow Hf isotopic range ($^{176}\text{Hf}/^{177}\text{Hf} = 0.282342\text{--}0.282462$; $\varepsilon_{\text{Hf}}(t) = -15.6$ to −12.8; $T_{\text{DM}}^{\text{C}} = 1.8$ to 2.0 Ga).

5.3. Major and trace element geochemistry

In this study, postcollisional volcanic rocks from the Xungba basin show high K_2O contents (4.36–9.00 wt.%) and $\text{K}_2\text{O}/\text{Na}_2\text{O}$ (1.64–6.16) (Table 2) with a wide compositional range from latite to rhyolite ($\text{SiO}_2 = 57.2\text{--}70.1$ wt.%) (Fig. 6a). Group 1 rocks are relatively more Mg-rich ($\text{MgO} = 4.57\text{--}6.75$ wt.%, $\text{Mg}^{\#} = 66.0\text{--}69.5$) and metaluminous ($\text{A/CNK} = 0.63\text{--}0.68$) (Fig. 5c), with high K_2O (5.69–6.82 wt.%) and $\text{K}_2\text{O}/\text{Na}_2\text{O}$ (2.62–3.34) (Fig. 6b). By contrast, Group 2 rocks are intermediate-silicic, showing varying $\text{K}_2\text{O}/\text{Na}_2\text{O}$ (1.64–6.16) but lower $\text{Mg}^{\#}$ (28.9–55.6), TiFe_2O_3 (2.52–4.09 wt.%), TiO_2 (0.55–1.02 wt.%), and P_2O_5 (0.14–0.38 wt.%), and wider range of A/CNK (0.90–1.16) (Table 2).

Overall, the Xungba K-rich rocks display a significant light REE (LREE) enrichment (Fig. 7a). The UPVR (Group 1) show a moderate LREE fractionation [$(\text{La/Sr})_{\text{N}} = 1.64\text{--}1.89$], a negative Eu anomaly ($\text{Eu/Eu}^* = 0.64\text{--}0.72$), a large $(\text{La/Yb})_{\text{N}}$ variation (22–27), and lower total REE contents ($\sum\text{REE} = 360\text{--}459$ ppm) (Table 2) (Fig. 7a), overlapping the field defined by postcollisional ultrapotassic rocks from the Lhasa terrane (cf. Zhao et al., 2009). The REE patterns of the PVR (Group 2) are comparable in light and middle REE patterns to Cambrian silicic lavas (Zhu et al., 2012a) and in HREEs [$(\text{La/Yb})_{\text{N}} = 30\text{--}74$] to S-type granites (Liu et al., 2006), both of which might originate from the Lhasa basement (Fig. 7a).

The most distinctive features of postcollisional Tibetan K-rich rocks are the pronounced enrichment in Th, U, K, and Pb, and relative depletion in Ba, Nb, Ta, Sr, and Ti (Fig. 7b). Aside from these similarities, the UPVR are characterized by high $(\text{Th/U})_{\text{N}}$ ratios (1.62–1.96), lower Hf/Sm ratios (0.55–0.62) (Table 2), more remarkably enrichment of K and weak depletion of Sr (Fig. 7b), falling into the field of postcollisional ultrapotassic magmatism in the Lhasa terrane (Fig. 7b) (cf. Zhao et al., 2009). As for the Xungba PVR, they have relatively lower abundances of incompatible and compatible elements than the UPVR, with strong Nb and Ta depletions, higher Hf/Sm ratios

Table 2

Whole-rock major and trace element compositions for postcollisional volcanic rocks from the Xungba Basin.

Sample No.	GJ0601	GJ0602	GJ0605	GJ0606	08YR04	GJ0614	GJ0617	GJ0619	GJ0620	GJ0624	GJ0627	GJ0628	GJ0629
Affinity	PVR												
TAS classification	Tr	Tr	Tr	Tr	Tr	Dac	Dac	Dac	Dac	TrD	TrD	TrD	TrD
<i>Major element (wt.%)</i>													
SiO ₂	63.1	63.3	62.7	63.5	65.1	68.9	68.1	68.4	70.1	68.5	68.3	66.9	67.4
TiO ₂	1.01	0.98	0.98	1.02	0.61	0.62	0.62	0.62	0.60	0.58	0.57	0.57	0.55
Al ₂ O ₃	15.2	15.2	15.4	15.8	15.9	15.4	15.2	15.3	15.3	15.2	15.0	15.0	15.0
TFe ₂ O ₃	3.90	3.96	3.93	4.09	2.87	3.07	2.96	3.01	2.63	2.52	2.77	2.72	3.02
MnO	0.03	0.03	0.05	0.02	0.03	0.01	0.05	0.05	0.02	0.03	0.04	0.05	0.04
MgO	2.08	1.93	2.48	1.38	1.45	0.63	1.47	1.52	0.66	1.48	1.57	1.50	1.55
CaO	2.76	2.54	2.74	1.90	2.55	2.63	2.41	2.42	2.49	2.31	2.21	2.83	2.43
Na ₂ O	1.48	1.53	1.52	1.46	2.58	2.61	2.42	2.48	2.53	2.52	2.45	2.76	2.42
K ₂ O	8.68	8.55	8.49	9.00	6.96	4.59	4.36	4.54	4.43	6.23	5.96	5.75	5.90
P ₂ O ₅	0.34	0.33	0.34	0.38	0.30	0.15	0.15	0.15	0.14	0.21	0.19	0.19	0.19
LOI	1.16	1.19	0.96	1.09	1.30	1.75	2.64	1.75	1.45	0.61	1.12	1.61	1.47
Total	99.8	99.6	99.6	99.6	99.6	100.3	100.4	100.2	100.4	100.2	100.2	99.8	100.1
K ₂ O/Na ₂ O	5.86	5.59	5.59	6.16	2.70	1.76	1.80	1.83	1.75	2.47	2.43	2.08	2.44
Mg [#]	51.4	49.1	55.6	40.1	50.0	28.9	49.6	50.0	33.2	53.8	52.9	52.2	50.4
A/CNK	0.90	0.93	0.93	1.01	0.97	1.09	1.16	1.14	1.14	1.01	1.04	0.94	1.02
A/NK	1.29	1.29	1.32	1.30	1.35	1.66	1.75	1.70	1.71	1.39	1.43	1.39	1.45
<i>Trace element (ppm)</i>													
Be	9.63	8.96	9.44	8.9	10.7	3.66	5.62	5.61	4.50	9.56	9.15	13.1	7.62
Sc	12.2	10.8	11.0	11.2	9.41	8.43	8.59	8.59	8.76	7.27	7.21	10.5	6.85
V	83.6	76.2	76.8	69.4	59.4	51.5	62.6	60.1	58.0	50.4	53.1	75.5	51.2
Cr	105	89.9	88.6	94.7	60.7	41.0	39.1	38.2	40.5	36.8	37.5	53.0	36.0
Co	9.09	7.56	9.73	8.43	7.69	2.69	4.86	4.81	4.48	7.11	6.34	9.32	6.21
Ni	18.2	17.0	11.9	18.7	15.0	6.77	4.77	4.18	7.08	10.5	10.4	15.2	10.3
Cu	18.5	21.0	11.6	14.8	20.0	6.16	8.38	5.89	8.59	7.61	10.4	14.7	8.89
Zn	83.8	68.9	77.4	67.1	68.5	44.9	68.8	69.5	52.0	63.5	61.1	93.4	60.5
Ga	26.6	25.5	26.5	27.0	25.6	27.4	27.4	27.1	27.0	26.2	26.7	39.9	26.6
Rb	457	442	419	465	399	319	314	310	301	395	414	585	397
Sr	491	487	508	505	479	211	190	193	183	318	301	498	334
Zr	563	562	603	570	377	267	268	268	286	271	256	398	228
Nb	31.9	31.2	32.6	33.0	20.3	13.2	12.6	12.9	12.4	21.1	20.4	30.2	19.9
Cs	121	35.6	52.5	54.9	34.4	20.7	20.8	20.6	18.5	35.8	30.7	50.9	21.2
Ba	1908	1892	1904	1984	1094	654	694	725	787	874	873	1333	875
Hf	17.4	16.6	17.7	17.1	10.3	7.80	7.82	7.68	8.07	8.34	7.86	12.00	7.09
Ta	3.55	3.40	3.50	3.54	2.08	1.14	1.06	1.11	1.03	1.98	1.95	2.96	1.87
Pb	85.9	88.1	90.7	90.4	106	39.0	37.1	39.1	34.9	82.9	79.8	122	75.6
Th	58.9	57.2	58.9	59.5	44.5	39.9	39.8	40.0	38.5	55.2	57.8	85.9	51.9
U	12.0	12.4	13.3	13.6	10.8	5.14	8.25	8.21	7.49	14.1	13.3	22.3	12.4
La	135	137	147	138	81.7	78.3	74.8	77.6	76.5	82.9	85.4	137	80.1
Ce	274	263	273	257	160	161	157	160	155	170	172	273	159
Pr	30.4	30.5	32.1	30.9	19.3	18.3	18.0	18.0	17.9	18.4	19.0	29.5	17.7
Nd	108	106	110	106	65.8	63.6	63.4	64.4	64.0	62.5	64.1	99.8	60.1
Sm	15.1	15.2	15.5	15.1	9.47	10.3	10.6	10.5	10.9	9.22	9.62	14.7	9.07
Eu	2.41	2.43	2.54	2.58	1.68	1.33	1.29	1.30	1.36	1.40	1.39	2.11	1.41
Gd _{corr}	7.62	7.97	8.14	7.93	5.07	6.00	6.23	6.24	6.54	4.91	5.09	7.64	4.83
Tb	0.86	0.92	0.94	0.91	0.59	0.73	0.76	0.76	0.81	0.57	0.59	0.87	0.56
Dy	3.78	3.91	4.10	3.90	2.57	3.42	3.70	3.97	4.15	2.55	2.67	3.91	2.50
Ho	0.65	0.66	0.68	0.63	0.43	0.62	0.69	0.69	0.75	0.44	0.43	0.69	0.42
Er	1.57	1.69	1.80	1.72	1.10	1.52	1.85	1.81	2.02	1.14	1.18	1.78	1.13
Tm	0.19	0.22	0.23	0.22	0.15	0.18	0.26	0.26	0.27	0.17	0.17	0.25	0.15
Yb	1.23	1.39	1.43	1.40	0.84	1.21	1.68	1.65	1.69	1.06	1.12	1.63	0.98
Lu	0.17	0.20	0.20	0.21	0.12	0.15	0.25	0.25	0.25	0.17	0.16	0.24	0.15
Y	16.7	17.8	18.5	17.8	11.7	16.5	18.8	18.9	20.3	12.0	12.5	18.7	12.0

(continued on next page)

Table 2 (continued)

Sample No.	10XB03	10XB04	10XB07	08YR05	10XB10	10XB12	10XB13	10YR01	10YR02	10YR04	10YR04 ^a	10YR07
Affinity	PVR	PVR	PVR	UPVR	UPVR							
TAS classification	Rhy	Rhy	TrD	Lat	Lat							
<i>Major element (wt.%)</i>												
SiO ₂	67.3	68.1	66.6	57.9	58.7	58.0	57.7	59.5	58.2	57.2	58.1	58.0
TiO ₂	0.62	0.62	0.63	1.06	1.19	1.19	1.21	1.21	1.13	1.15	1.13	1.15
Al ₂ O ₃	14.8	15.3	15.0	12.8	13.1	13.0	12.7	13.6	13.1	12.7	12.7	12.9
TFe ₂ O ₃	3.08	2.91	3.25	6.09	5.38	5.80	5.87	3.98	5.34	5.90	5.72	5.85
MnO	0.05	0.02	0.05	0.09	0.08	0.09	0.09	0.07	0.08	0.09	0.09	0.10
MgO	1.27	0.91	1.65	6.75	5.28	6.29	6.31	4.57	5.64	6.63	6.26	6.58
CaO	2.01	2.50	2.42	5.32	4.62	4.96	5.06	5.77	5.90	5.51	5.15	5.34
Na ₂ O	2.35	2.95	2.60	2.17	2.28	2.23	2.15	2.01	2.05	1.87	1.91	1.90
K ₂ O	5.06	4.85	5.11	5.69	6.57	6.82	6.63	6.52	5.76	6.13	6.37	6.30
P ₂ O ₅	0.21	0.16	0.23	0.79	0.80	1.01	0.97	1.16	0.91	1.02	0.95	1.07
LOI	2.56	1.02	1.89	1.06	1.35	1.02	1.07	1.14	1.52	1.58	1.31	1.02
Total	99.3	99.4	99.4	99.7	99.3	100.4	99.8	99.6	99.6	99.8	100.2	100.2
K ₂ O/Na ₂ O	2.16	1.64	1.97	2.62	2.89	3.06	3.08	3.24	2.81	3.28	3.34	3.31
Mg [#]	45.1	38.1	50.0	68.7	66.0	68.2	68.1	69.5	67.7	69.0	68.9	69.0
A/CNK	1.14	1.05	1.06	0.66	0.68	0.65	0.64	0.65	0.64	0.65	0.63	0.66
A/NK	1.58	1.52	1.53	1.31	1.21	1.17	1.19	1.31	1.36	1.31	1.27	1.30
<i>Trace element (ppm)</i>												
Be	7.32	7.06	7.38	7.21	9.89	10.1	10.0	7.16	6.52	7.05	6.76	7.45
Sc	7.27	7.37	7.56	16.6	15.6	16.3	16.3	16.8	16.0	15.7	15.4	15.5
V	51.5	54.1	60.2	131	112	109	110	139	131	130	126	127
Cr	33.2	35.6	41.3	318	475	517	510	375	334	329	296	325
Co	5.33	4.66	6.62	26.8	24.6	25.7	27.3	14.6	20.9	28.2	27.1	25.4
Ni	13.6	9.69	10.2	179	240	234	256	80.6	147	233	230	192
Cu	9.82	12.7	12.2	44.8	52.3	37.3	23.3	38.1	45.9	47.7	45.9	43.6
Zn	84.8	80.5	84.0	75.9	66.9	75.1	74.3	84.3	81.0	77.9	75.4	78.9
Ga	29.2	30.8	29.5	20.5	21.8	22.0	21.3	21.6	20.0	20.1	19.6	20.2
Rb	337	354	341	527	453	477	456	540	450	518	511	523
Sr	167	205	192	659	755	741	734	682	637	640	624	636
Zr	266	269	266	390	496	508	513	433	392	405	395	407
Nb	11.5	10.2	9.85	24.4	34.1	36.3	37.4	26.9	23.8	25.7	24.6	25.0
Cs	19.0	19.1	19.6	29.9	28.0	32.7	30.1	33.8	16.9	32.0	31	31.8
Ba	638	650	566	1982	2080	2208	2175	2001	1786	1827	1760	1824
Hf	7.41	7.40	7.59	10.9	14.6	15.2	15.3	11.9	10.8	11.1	10.8	11.0
Ta	0.86	0.75	0.72	1.29	1.96	2.17	2.17	1.38	1.25	1.30	1.27	1.30
Pb	38.3	39.1	38.5	46.8	86.6	87.2	83.0	57.4	41.5	46.2	46.0	46.5
Th	40.4	42.9	41.9	135	116	127	123	140	122	131	131	131
U	8.84	7.40	8.61	17.9	17.8	16.0	16.8	21.1	16.8	17.5	17.4	17.4
La	76.4	87.1	77.9	57.9	64.4	67.2	65.6	61.2	55.8	57.4	55.7	57.3
Ce	161	170	166	141	176	182	178	153	142	144	141	143
Pr	20.5	23.3	20.9	21.4	27.9	29.5	29.0	24.4	22.0	22.5	22.6	22.4
Nd	69.3	78.6	71.9	96.3	128	135	132	113	97.9	98.0	93.8	105
Sm	11.9	13.1	12.0	20.0	23.8	25.8	24.6	21.3	18.6	19.9	19.5	19.8
Eu	1.24	1.28	1.16	3.28	3.60	3.89	3.76	3.28	3.02	3.12	3.10	3.11
Gd _{corr}	7.20	7.41	6.87	9.7	12.4	13.6	13.1	10.8	9.8	10.0	9.92	9.9
Tb	0.89	0.89	0.83	1.07	1.42	1.56	1.51	1.22	1.13	1.12	1.12	1.12
Dy	3.87	3.53	3.27	4.58	5.58	6.19	5.94	5.02	4.56	4.49	4.38	4.47
Ho	0.64	0.55	0.52	0.82	0.84	0.91	0.91	0.81	0.75	0.71	0.70	0.69
Er	1.81	1.53	1.47	2.05	2.31	2.48	2.39	2.36	2.20	2.11	2.04	1.99
Tm	0.24	0.19	0.19	0.29	0.27	0.29	0.28	0.29	0.28	0.26	0.24	0.26
Yb	1.40	1.19	1.14	1.76	1.59	1.70	1.69	1.70	1.60	1.53	1.50	1.56
Lu	0.21	0.16	0.17	0.25	0.24	0.24	0.24	0.25	0.26	0.24	0.23	0.23
Y	18.5	16.4	15.0	22.7	24.9	27.3	26.6	24.3	22.6	21.7	21.3	21.4

TAS, total alkalis vs. silica; Tr, trachyte; TrD, trachydacite; Lat, latite; Dac, dacite; Rhy, rhyolite. LOI, loss on ignition.

Gd_{corr} = 0.259 × $\sqrt[3]{\text{Sm}_N \times \text{Tb}_N}$, Sm_N and Tb_N were chondrite-normalized (Boynton, 1984).

Mg[#] = Mg²⁺/(Mg²⁺ + Fe²⁺) (molar ratio); A/CNK = Al₂O₃/(CaO + Na₂O + K₂O) (molar ratio); A/NK = Al₂O₃/(Na₂O + K₂O) (molar ratio).

^a Duplicate for showing analytical precision.

Table 3
Whole-rock Sr–Nd–Pb–O isotopic compositions for Xungba postcollisional volcanic rocks.

Sample No.	$\delta^{18}\text{O}_{\text{V-SMOW}}$ (‰)	Rb (ppm)	Sr (ppm)	$^{87}\text{Sr}/^{86}\text{Sr}$		Sm (ppm)	Nd (ppm)	$^{143}\text{Nd}/^{144}\text{Nd}$		$^{143}\text{Nd}/^{144}\text{Nd}_{(i)}$	$\varepsilon_{\text{Nd}}(t)$	T_{DM} (Ga)	$^{206}\text{Pb}/^{204}\text{Pb}$	$^{207}\text{Pb}/^{204}\text{Pb}$	$^{208}\text{Pb}/^{204}\text{Pb}$	
				Ratio	$\pm 2\sigma$			Ratio	$\pm 2\sigma$							
GJ0601	13.0	456.8	491.3	0.740593	11	0.7397	15.1	108.1	0.511957	13	0.511944	-13.0	1.41	18.825	15.788	39.609
GJ0602	13.1	442.2	486.8	0.739577	11	0.7387	15.2	106.0	0.511958	13	0.511945	-12.9	1.43	18.824	15.787	39.604
GJ0605	12.8	419.2	508.4	-	-	-	15.5	110.5	0.511965	13	0.511952	-12.8	1.40	18.828	15.788	39.611
GJ0606	13.7	465.4	504.9	0.739035	10	0.7382	15.1	105.9	0.511985	13	0.511972	-12.4	1.39	18.831	15.789	39.608
08YR04	-	399.3	478.7	0.735859	6	0.7351	9.5	65.8	0.511952	8	0.511939	-13.1	1.44	18.826	15.782	39.586
GJ0614	12.3	319.0	211.4	0.734442	12	0.7330	10.3	63.6	0.511911	13	0.511896	-13.9	1.63	18.859	15.795	39.725
GJ0617	12.5	314.3	189.7	0.736300	9	0.7347	10.6	63.4	0.511903	10	0.511888	-14.1	1.69	18.876	15.797	39.737
GJ0619	-	310.1	192.6	0.735886	9	0.7344	10.5	64.4	0.511898	12	0.511883	-14.1	1.66	18.874	15.796	39.733
GJ0620	-	301.5	183.3	0.732696	11	0.7311	10.9	64.0	0.511898	11	0.511883	-14.2	1.71	18.875	15.796	39.736
GJ0624	-	395.1	317.7	0.733256	10	0.7321	9.2	62.5	0.511950	12	0.511937	-13.1	1.47	18.813	15.786	39.621
GJ0627	-	413.9	300.5	0.732916	9	0.7316	9.6	64.1	0.511954	13	0.511940	-13.0	1.48	18.813	15.785	39.630
GJ0628	10.5	584.7	497.7	0.732819	12	0.7317	14.7	99.8	0.511962	10	0.511949	-12.9	1.45	18.811	15.784	39.623
GJ0629	9.4	397.3	334.2	0.732739	11	0.7316	9.1	60.1	0.511955	11	0.511941	-13.0	1.49	18.808	15.785	39.627
10XB03	11.6	337.2	167.4	0.740400	4	0.7385	11.9	69.3	0.511879	2	0.511863	-14.5	1.76	18.909	15.754	39.659
10XB04	13.0	354.4	205.5	0.730801	6	0.7292	13.1	78.6	0.511903	3	0.511888	-14.1	1.68	18.866	15.742	39.610
10XB07	-	341.2	191.7	0.731030	5	0.7293	12.0	71.9	0.511913	3	0.511898	-13.9	1.67	18.843	15.717	39.515
08YR05	-	526.9	658.7	0.718822	4	0.7181	20.0	96.3	0.511924	4	0.511905	-13.7	2.12	18.671	15.751	39.745
10XB10	11.3	453.3	754.9	0.717902	4	0.7173	23.8	127.9	0.512008	3	0.511991	-12.0	1.72	18.695	15.684	39.306
10XB12	10.1	476.5	740.9	0.720027	6	0.7194	25.8	135.5	0.511977	2	0.511960	-12.7	1.81	-	-	-
10XB13	-	456.0	734.3	0.720312	4	0.7197	24.6	131.5	0.511978	3	0.511961	-12.6	1.77	18.691	15.696	39.358
10YR01	12.3	540.3	682.3	0.719501	4	0.7188	21.3	112.6	0.511921	2	0.511904	-13.7	1.88	18.630	15.680	39.483
10YR02	11.0	450.3	636.6	0.718966	7	0.7183	18.6	97.9	0.511933	2	0.511916	-13.5	1.87	18.646	15.698	39.576
10YR04	11.3	518.4	640.0	0.719616	5	0.7188	19.9	98.0	0.511923	3	0.511905	-13.7	2.05	18.641	15.700	39.580
10YR07	10.1	523.4	636.1	0.719596	5	0.7188	19.8	104.7	0.511923	2	0.511906	-13.7	1.88	18.633	15.690	39.547

Table 4
Isotopic compositions of melts derived from three geochemistry end-members.

Geochemistry end-members	SCLM	Hypothetical ancient lower crust	Ancient Lhasa basement
Rb (ppm)	26.3	—	136.6
Sr (ppm)	1027	300	77.2
$^{87}\text{Sr}/^{86}\text{Sr}$	0.705	0.710	0.756
Sm (ppm)	7.06	—	5.72
Nd (ppm)	40.3	26.0	28.8
$^{143}\text{Nd}/^{144}\text{Nd}$	0.5126	0.5115	0.5119
$\delta^{18}\text{O}_{\text{V-SMOW}} (\text{\textperthousand})$	5.3 ± 0.4	≤ 5.3	9.5–14

The concentrations of Rb, Sr, Sm and Nd, together with Sr–Nd isotopic compositions for these three end-members, are averages based on Miller et al. (1999), Ding et al. (2003), and Zhu et al. (2012a). Pb concentrations and $^{206}\text{Pb}/^{204}\text{Pb}$ ratios are from Zhao et al. (2007). Oxygen isotopic composition of ancient Lhasa basement was converted from zircon oxygen isotopic ratios from sample 08DX17 in Zhu et al. (2012b) [$\delta^{18}\text{O}(\text{WR}) = \delta^{18}\text{O}(\text{Zrc}) + 0.0612 \times \text{SiO}_2 - 2.5$; (Valley et al., 2005)].

(0.62–1.15), and negative Sr and P anomalies (Fig. 7b) (Table 2).

5.4. Sr–Nd–Pb–O isotopic geochemistry

The Xungba lavas show a broad range of Sr isotope ($^{87}\text{Sr}/^{86}\text{Sr}_{(i)} = 0.7173\text{--}0.7397$), but relatively narrow range of Nd isotopic ratios ($^{143}\text{Nd}/^{144}\text{Nd}_{(i)} = 0.5119\text{--}0.5120$) (Table 3). The Sr–Nd isotopic compositions of the Xungba UPVR ($^{87}\text{Sr}/^{86}\text{Sr}_{(i)} = 0.7173\text{--}0.7197$; $^{143}\text{Nd}/^{144}\text{Nd}_{(i)} = 0.5119\text{--}0.5120$) plot within the field of middle-late Miocene ultrapotassic rocks in the central Lhasa subterrane, but diverge from the trend defined by ultrapotassic rocks outcropping in the southern Lhasa subterrane (Fig. 8a) (cf. Williams et al., 2004; Gao et al., 2007; Zhao et al., 2009). In comparison, the Xungba PVR display different Sr–Nd isotopes with higher radiogenic Sr

($^{87}\text{Sr}/^{86}\text{Sr}_{(i)} = 0.7291\text{--}0.7385$) and similar unradiogenic Nd isotopic compositions ($^{143}\text{Nd}/^{144}\text{Nd}_{(i)} = 0.5119\text{--}0.5120$) (Table 3), which in effect fill in the Sr–Nd isotopic composition gap between coeval potassic rocks in central Lhasa subterrane and the geochemistry end-member of ancient Lhasa basement/Himalayan basement (Fig. 8a).

Both Group 1 and 2 volcanic rocks plot above the Northern Hemisphere Reference Line (NHRL), showing highly radiogenic Pb isotopic signatures ($^{206}\text{Pb}/^{204}\text{Pb} = 18.63\text{--}18.91$, $^{207}\text{Pb}/^{204}\text{Pb} = 15.68\text{--}15.80$, $^{208}\text{Pb}/^{204}\text{Pb} = 39.31\text{--}39.75$) (Table 3) in common with postcollisional rocks in the Lhasa terrane (Fig. 8b and c). Although the Pb isotopic compositions of Lhasa and Himalaya basement partially overlap, the Xungba UPVR and PVR have relatively low $^{206}\text{Pb}/^{204}\text{Pb}$, showing a significant Lhasa terrane crustal affinity.

The whole-rock oxygen isotopic compositions of the PVR and UPVR are different (Table 3). The $\delta^{18}\text{O}_{\text{V-SMOW}}$ value of UPVR ranges from 10.1 to 12.3, similar to those from the western Lhasa terrane (Miller et al., 1999), but higher than other postcollisional rocks (27–11 Ma; $\delta^{18}\text{O}_{\text{V-SMOW}} = 6.3\text{--}10.3\text{\textperthousand}$; Ding et al., 2006; Zhao et al., 2009). Oxygen isotopic compositions of the PVR (9.4–13.7‰) are close to that of the granitoids derived from Lhasa basement ($\delta^{18}\text{O}_{\text{V-SMOW}} = 8.9\text{--}13.3\text{\textperthousand}$, Table 3), which are overall more enriched than the associated UPVR (Fig. 9a).

6. DISCUSSION

6.1. Petrogenesis of ultrapotassic volcanic rocks from Lhasa terrane

Tibetan ultrapotassic rocks are characterized by high-MgO and compatible element contents, high Rb/Sr and low Ba/Rb (not shown) (Turner et al., 1996; Miller et al., 1999; Ding et al., 2003; Williams et al., 2004; Zhao et al., 2009), which is consistent with derivation from a phlogopite-bearing mantle source. This interpretation is supported by the phlogopite-bearing spinel facies xenoliths

Table 5
Mineral/melt partition coefficients used in the trace element modeling.

Phlogopite-spinel Iherzolite	Ol	Opx	Cpx	Phl	Spl	Whole-rock partition coefficients
						Ol(0.70) + Opx(0.15) + Cpx(0.09) + Phl (0.05) + Spl (0.01)
D _{La}	0.0000046	0.00057	0.0586	0.0004	—	0.00538
D _{Dy}	0.0053	0.0365	0.5382	0.0182	—	0.05850
D _{Yb}	0.0214	0.2075	0.5819	0.0330	—	0.10013
Rutile-bearing eclogite	Grt	Cpx	Rt			Grt(0.64) + Cpx (0.35) + Rt(0.01) Grt(0.35) + Cpx (0.64) + Rt(0.01)
D _{La}	0.0027	0.0281	0.3000			0.3216 0.0219
D _{Dy}	2.6594	0.4588	0.0280			1.901 1.225
D _{Yb}	10.0544	0.5983	0.0120			6.666 3.902

These mineral–melt D values (partition coefficients) are averages of available data for different phases. (1) In spinel facies Iherzolite, the partition coefficients for Ol are from McDade et al. (2003) and Lee et al. (2007). D values of Opx and Phl are from Grégoire et al. (2000) and Sun and Liang (2012), respectively. (2) In rutile-bearing eclogitic facies, partition coefficients for Grt are from Green et al. (2000) and Pertermann et al. (2004), and, for Cpx, D values are from Pertermann and Hirschmann (2002) and Pertermann et al. (2004). D values of Rt are based on Pilet et al. (2011).

Values in brackets denote the mineral percentages in the residue.

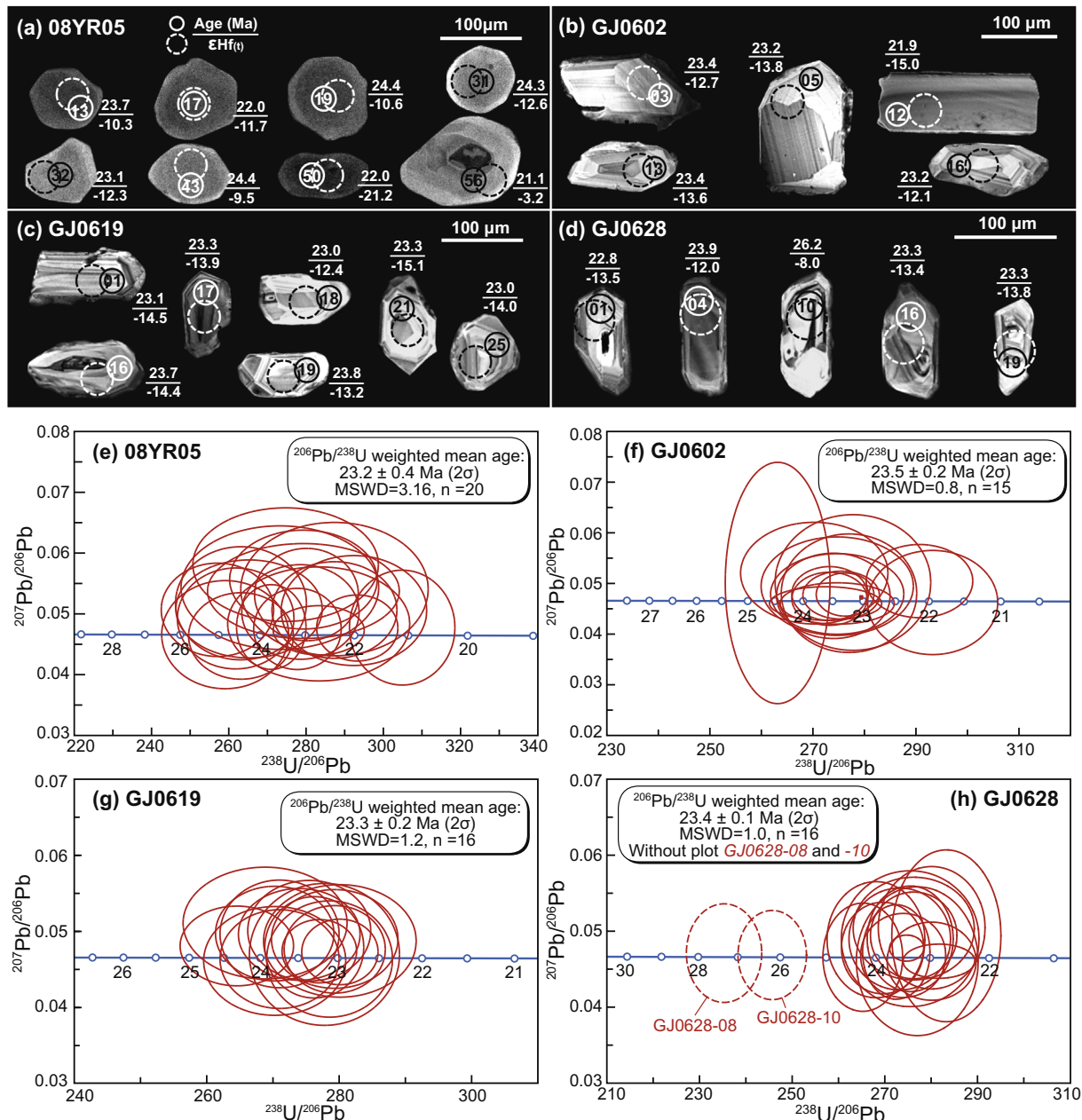


Fig. 4. (a-d) Cathodoluminescence images, and (e-h) Tera–Wasserburg diagrams for zircons from Xungba potassic and ultrapotasssic rocks.

found in the UPVR in the Sailipu basin (Zhao et al., 2008; Liu et al., 2011a). The consistence between REE patterns of the UPVR and the model melts in equilibrium with clinopyroxenes in the mantle xenolith (Liu et al., 2011a) further corroborates that the ultrapotasssic melt is originated from a phlogopite–clinopyroxene–olivine assemblage mantle source represented by the lherzolite/harzburgite mantle xenoliths (i.e., metasomatized lithospheric mantle origin). As the Xungba early-Miocene UPVR share the same geochemical characteristics mentioned above, it is reasonable to assume the same lithospheric mantle origin.

However, compared with basalts, the relatively high silica contents of the UPVR cannot be formed alone by partial melting of hydrous spinel-facies peridotites even if the

mantle beneath southern Tibet had experienced protracted hydration during Tethyan oceanic subduction. Because partial melts produced in the hydrous spinel stability field (1100–1400 °C; 1.2–2.0 GPa) are still basaltic with only 1–3 wt.% SiO₂ increase even though the H₂O content can be up to 6.3 wt.% (cf. Gaetani and Grove, 1998).

Although ultrapotasssic rocks can form in various tectonic settings (Müller et al., 1992), crustal material always plays an important role in ultrapotasssic magma evolution (Avanzinelli et al., 2009; Conticelli et al., 2009a,b). In the Lhasa terrane, the UPVR commonly display continental-crust-like geochemical features (e.g., enriched Sr–Nd–Pb–O isotopes) (Miller et al., 1999; Williams et al., 2004; Zhao et al., 2009). The extensive fractional crystallization

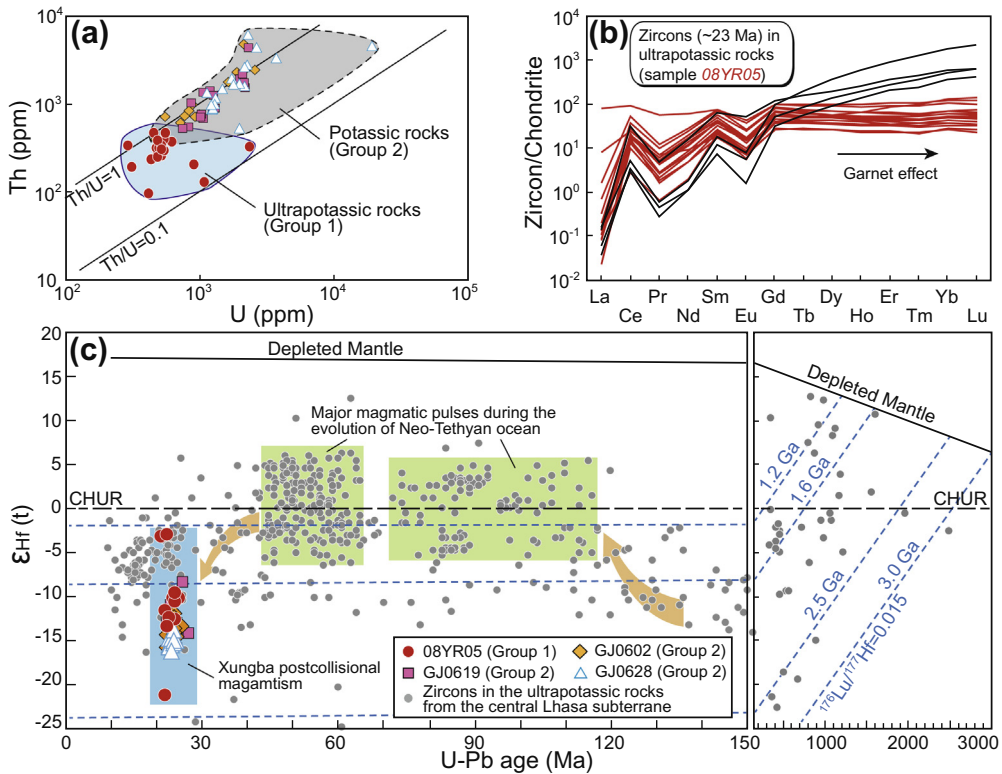


Fig. 5. Plots of (a) Th vs. U of zircon, (b) chondrite-normalized REE patterns for zircons from UPVR sample 08YR05 (normalizing data from Boynton, 1984), and (c) zircon $\epsilon_{\text{Hf}}(t)$ vs. U–Pb age. The Hf isotope and U–Pb ages for zircons in the Tibetan ultrapotassic rocks are from Liu et al. (2014). DM and CHUR denote a generalized depleted mantle growth curve and chondrite reference, respectively.

can be ruled out as the major cause of SiO_2 elevation because the steep positive La/Yb–La correlation is consistent with varying extent of partial melting rather than fractional crystallization (Fig. 10a). Therefore, partial melting of metasomatized mantle lithosphere and the melt modified by Lhasa terrane crust assimilation during ascent altogether readily explain the petrogenesis of the UPVR. The metasomatism may have genetically associated with Neo-Tethyan subduction involving seafloor sediments and/or terrigenous sediments (e.g., Himalayan basement, i.e., the northern margin of the Indian continent) (Miller et al., 1999; Ding et al., 2003; Williams et al., 2004; Guo et al., 2006, 2013; Gao et al., 2007; Zhao et al., 2009).

6.1.1. Enriched isotopic compositions and crustal contamination by ancient Lhasa basement

Because of the differences in crustal composition between the central and southern Lhasa subterrane (Zhu et al., 2011a, 2013), and because of the spatial distribution of ultrapotassic magmatism mentioned above (Fig. 1a), we infer that the crust must have contributed to the postcollisional magmatism in southern Tibet. Many lines of evidence support this inference: (i) the majority of the UPVR are localized in the central Lhasa subterrane with only a few ultrapotassic veins found in the southern Lhasa subterrane; (ii) compared with the juvenile crusts in the northern and southern Lhasa subterrane (Zhu et al., 2011a), the central Lhasa subterrane has an old basement of Proterozoic and Archean age (zircon Hf model ages up

to 2870 Ma; Dong et al., 2010; Zhu et al., 2011a,b); (iii) Paleozoic–Proterozoic zircon xenocrysts have been found in the UPVR (Fig. 5c; Sun et al., 2008; Liu et al., 2011b, 2014); (iv) the least radiogenic Hf isotopic composition of co-magmatic zircons from the UPVR overlaps that of Lhasa basement (Fig. 5c). Together with the crustal xenoliths widely identified from the ultrapotassic rocks (Fig. 3a; Miller et al., 1999; Hébert et al., 2014; Liu et al., 2014), all the above data and observations signify the contribution of the ancient Lhasa basement (upper-middle crust) to the petrogenesis of the UPVR.

In the plot of $\delta^{18}\text{O}_{\text{V-SMOW}}$ vs. $^{87}\text{Sr}/^{86}\text{Sr}$ (Fig. 9a), which is often used to assess the extent of crustal contamination in source regions (cf. Macpherson et al., 1998), the UPVR plot on strongly convex-upward hyperbolas consistent with mixing between lithospheric mantle and ancient Lhasa basement. This process also accounts for the negative correlation between $\delta^{18}\text{O}_{\text{V-SMOW}}$ and MgO in UPVR samples with MgO > 6 wt.% (Fig. 9b). The increasingly $^{87}\text{Sr}/^{86}\text{Sr}$ with decreasing MgO (Fig. 9c) lends further support for the crustal contamination interpretation. In addition, the petrography also point to the importance of the crustal contamination. For example, crystallization of pyroxenes (both Opx and Cpx) at the expense of olivine is a straightforward consequence of the reaction of the form olivine + SiO_2 = pyroxenes as a result of crustal contamination (addition of crustal SiO_2) or magma mixing (addition of SiO_2 from the induced crustal melt) (Fig. 3d–f). Therefore, the enriched isotopic signatures of the Tibetan

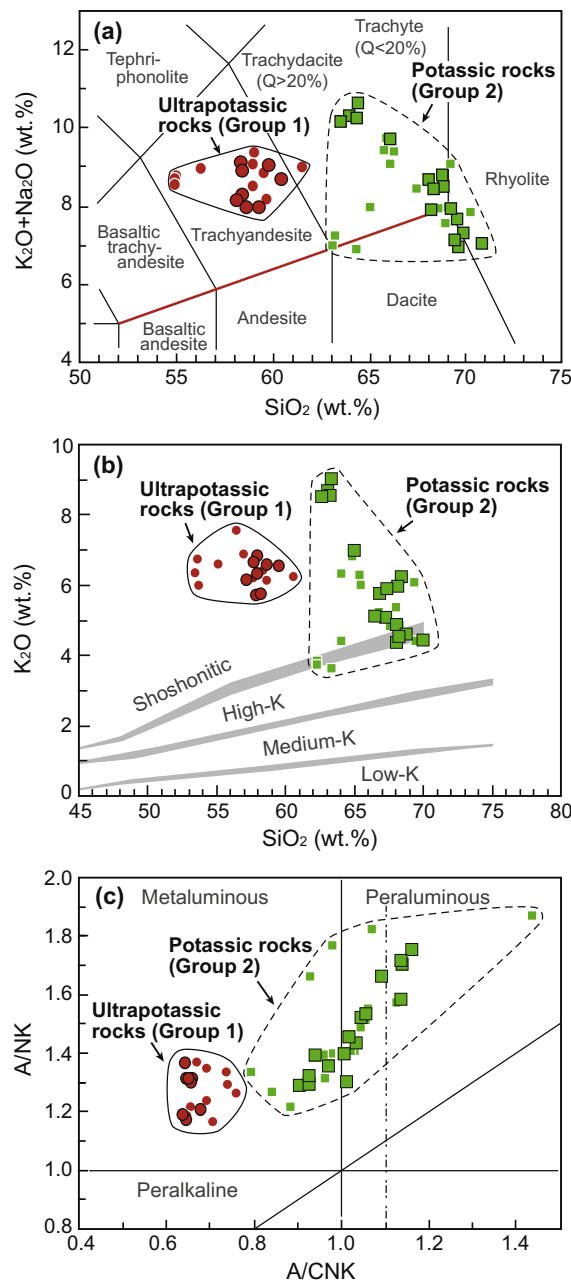


Fig. 6. Classification diagrams of the Xungba postcollisional volcanic rocks: (a) Total alkalis vs. SiO_2 (Le Maitre et al., 2005), (b) K_2O vs. SiO_2 , and (c) A/NK vs. A/CNK . The smaller red circles and green squares are data from the literature (Miller et al., 1999; Chen et al., 2011; Liu et al., 2011b). (For interpretation of the references to color in this figure legend, the reader is referred to the web version of this article.)

ultrapotassic rocks may be partially derived from the ancient crust of the Lhasa terrane.

6.1.2. “Garnet-signature” and material input from thickened lower crust

Crustal contamination by ancient Lhasa basement can produce extremely enriched isotopic composition of ultrapotassic magmas (Fig. 9). We show here the deep crust

can also contribute to the petrogenesis of the UPVR. The positive La/Yb - Dy/Yb correlation defined by the UPVR (Fig. 10b) indicates the presence of garnet as a residual phase in the source region (cf. Miller et al., 1999; Zhao et al., 2009). Previously, the “garnet-signature” in the UPVR was widely regarded as melt input from melting of garnet facies mantle lithosphere because melts derived from spinel facies mantle cannot explain the large HREE fractionation (i.e., high Dy/Yb ratios, Miller et al., 1999; Zhao et al., 2009; Prelević et al., 2012). However, it seems unlikely that the “garnet-signature” in the UPVR to have derived from partial melts from the garnet-facies mantle. This is because partial melting of garnet peridotite, even in hydrous condition ($\text{H}_2\text{O} = 1.5\text{--}5\text{ wt.}\%$; $1200\text{--}1450\text{ }^\circ\text{C}$; 3.5 GPa), generates SiO_2 -poor but MgO -rich melts (cf. Tenner et al., 2012) and these melts commonly display higher $\text{CaO}/\text{Al}_2\text{O}_3$, yet it is unobserved (Fig. 10c). In addition, mantle xenoliths (e.g., Sailipu xenoliths), which were thought to be fragments of mantle sources of the ultrapotassic magmas (Zhao et al., 2008; Liu et al., 2011a), are derived from depths of 50–65 km that is shallower than the spinel-garnet transition depth (Liu et al., 2011a). Overall, additional components with low $\text{CaO}/\text{Al}_2\text{O}_3$ and high SiO_2 are required for the petrogenesis of the UPVR (Fig. 10c).

Recent studies suggest that the pyroxene-rich veins or layers (i.e., olivine-poor pyroxenite, garnet pyroxenite or eclogite) may be the possible magma sources of alkali magmas (Hirschmann and Stolper, 1996; Hirschmann et al., 2003; Keshav et al., 2004; Sobolev et al., 2005). Moreover, partial melting of pyroxene-rich lithologies can impart the “garnet signature” independent of the great depth required by garnet-facies peridotite melting (Hirschmann and Stolper, 1996) and produce melts with moderate MgO and relatively high SiO_2 (Kogiso et al., 2003; Keshav et al., 2004). However, partial melts derived from mantle pyroxenite (without olivine) would generate magmas with high SiO_2 (up to 55%) but high Ni/MgO (Sobolev et al., 2005, Herzberg, 2006), which cannot explain the low Ni/MgO and high SiO_2 ultrapotassic rocks in the Lhasa terrane (Fig. 10d). Also, some partial melts of garnet pyroxenite, in experiments, are too aluminous to be appropriate for the UPVR (Hirschmann et al., 2003; Kogiso et al., 2003).

Thickened lower crust (eclogite-facies or garnet-bearing granulite-facies) could be another candidate to explain the “garnet-signature” (Spandler et al., 2008; Wang et al., 2010) (Fig. 10b), especially when the continued thickening associated with the Indian–Asia convergence since the Eocene is taken into consideration (Chung et al., 2005, 2009). Compared with the contribution of garnet-facies mantle-derived melts, melt derived from the eclogitic lower crust would have high SiO_2 and low MgO , $\text{CaO}/\text{Al}_2\text{O}_3$, and Ni/MgO (Sobolev et al., 2005; Spandler et al., 2008; Wang et al., 2010). What’s more, the positive trends between Sr–O isotopic ratios and MgO also support a potential contribution from the lower crust that is characterized by low $^{87}\text{Sr}/^{86}\text{Sr}$ and $\delta^{18}\text{O}_{\text{V-SMOW}}$ values (Fig. 9b and c). Other lines of evidence supporting lower crust contribution include: (i) the close spatial association between

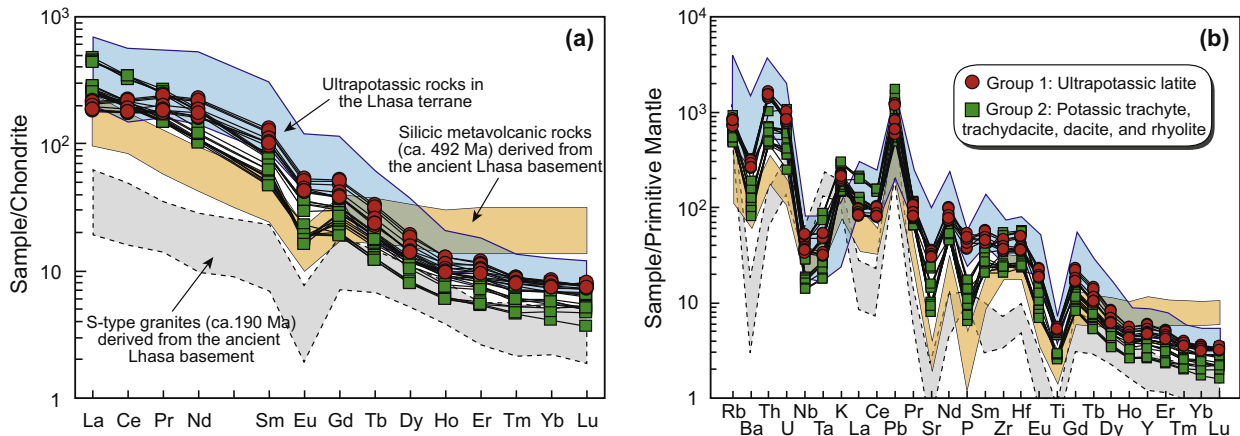


Fig. 7. (a) Chondrite normalized REE patterns, and (b) primitive mantle normalized trace element patterns for Xungba volcanic rocks. Chondrite and primitive mantle values are from Boynton (1984) and Sun and McDonough (1989), respectively. Shaded fields of Miocene UPVR are from Zhao et al. (2009), and data of the Cambrian silicic metavolcanic rocks and Jurassic S-type granitoids are from Zhu et al. (2012a) and Liu et al. (2006).

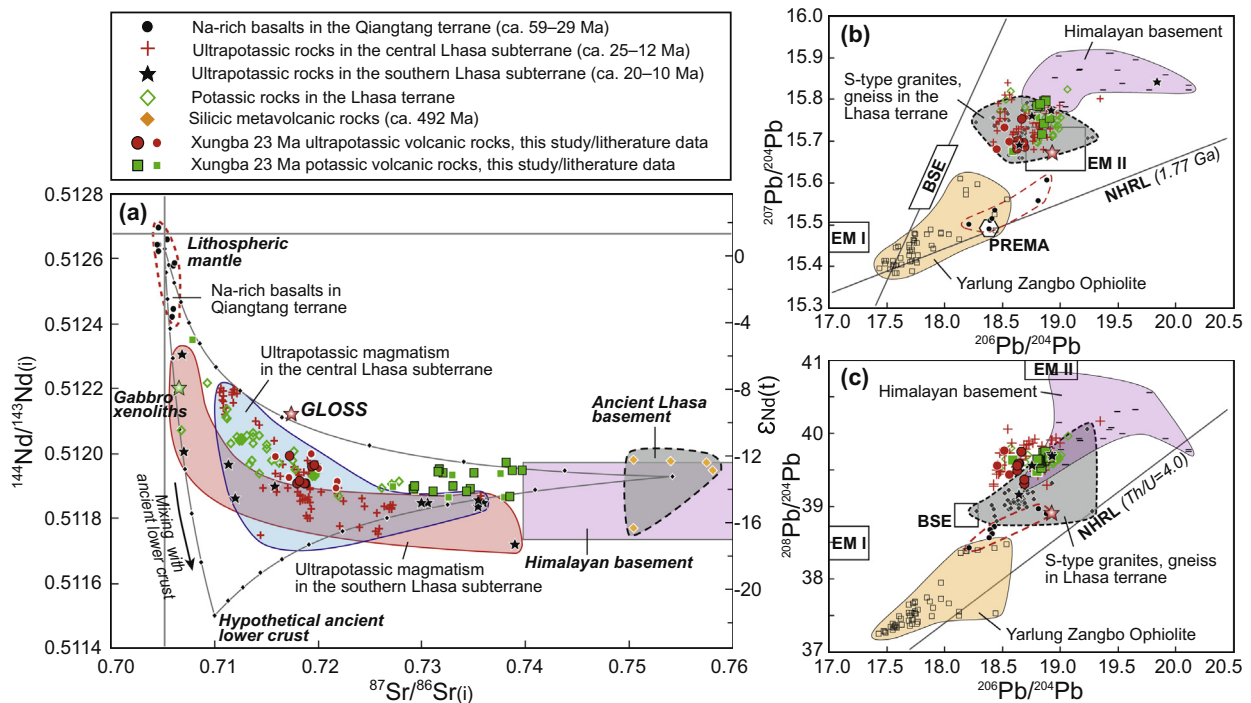


Fig. 8. (a) Plot of initial $^{143}\text{Nd}/^{144}\text{Nd}_{(i)}$ vs. $^{87}\text{Sr}/^{86}\text{Sr}_{(i)}$ for postcollisional magmatic rocks in the Lhasa terrane. (b and c) Plots of lead isotopic ratios: (b) $^{207}\text{Pb}/^{204}\text{Pb}$ vs. $^{206}\text{Pb}/^{204}\text{Pb}$ and (c) $^{208}\text{Pb}/^{204}\text{Pb}$ vs. $^{206}\text{Pb}/^{204}\text{Pb}$. Qiangtang Na-rich basalts (cf. Ding et al., 2003), the PVR–UPVR in the Lhasa terrane (see references in Fig. 1), ancient Lhasa basement (Zhu et al., 2012a), GLOSS (Plank and Langmuir, 1998), gabbroic xenolith entrained by ultrapotassic magma (Miller et al., 1999), and Himalayan basement (Zhao et al., 2009) are illustrated shown for comparison. Isotopic compositions of three geochemistry end-members are given in Table 4. Three calculated isotopic mixing hyperbolas with 10% intervals are also shown for comparison. Bulk Silicate Earth (BSE), enriched mantle components (EM I and EM II) and prevalent mantle (PREMA) are from Zindler and Hart (1986). Northern Hemisphere Reference Line (NHRL): $^{207}\text{Pb}/^{204}\text{Pb} = 0.1084 \times ^{206}\text{Pb}/^{204}\text{Pb} + 13.491$; $^{208}\text{Pb}/^{204}\text{Pb} = 1.209 \times ^{206}\text{Pb}/^{204}\text{Pb} + 15.627$. Other data sources are illustrated for showing the crustal affinity of the PVR–UPVR in the Lhasa terrane: Yarlung Zangbo ophiolite (Göpel et al., 1984; Mahoney et al., 1998; Xu and Castillo, 2004; Zhang et al., 2005; Niu et al., 2006), granitoids derived from ancient Lhasa basement (Gariépy et al., 1985; Liao, 2003), and Himalayan basement (Vidal et al., 1982; Göpel et al., 1984). $^{87}\text{Sr}/^{86}\text{Sr}_{(i)}$, $^{143}\text{Nd}/^{144}\text{Nd}_{(i)}$, and $\varepsilon_{\text{Nd}}(t)$ are corrected to 23 Ma.

ultrapotassic and adakitic rocks (Chen et al., 2011, 2012), (ii) gabbro and granulite xenoliths identified in the UPVR,

which may represent the contribution from juvenile crust (Miller et al., 1999; Chan et al., 2009; Liu et al., 2014),

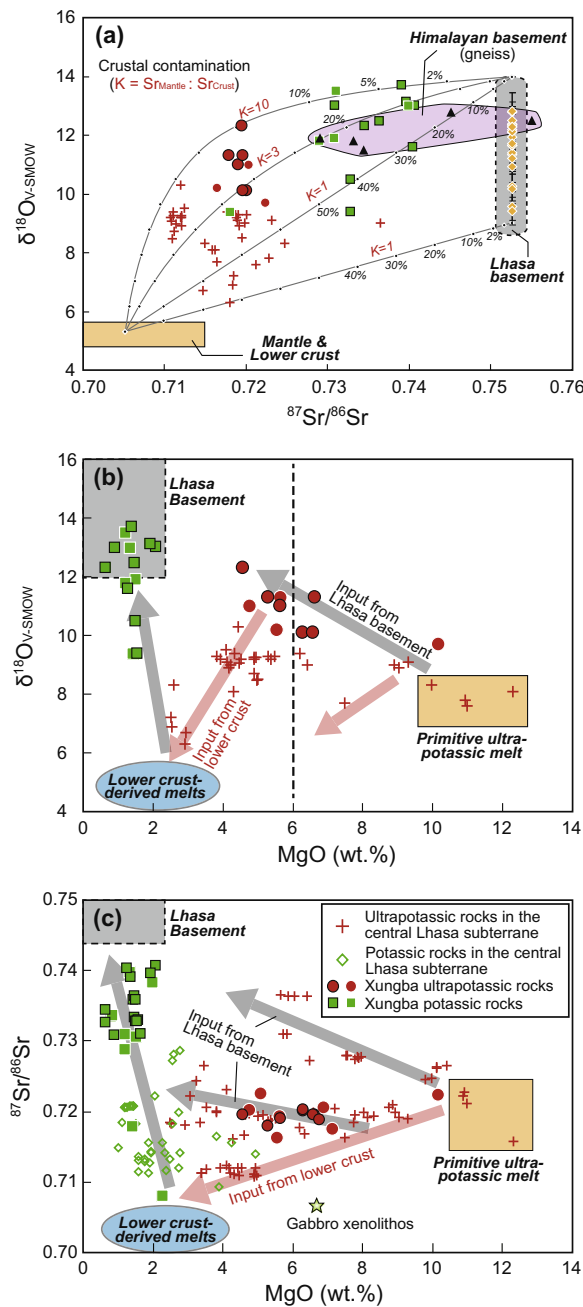


Fig. 9. Plots of (a) $\delta^{18}\text{O}_{\text{v-SMOW}}$ vs. ${}^{87}\text{Sr}/{}^{86}\text{Sr}$, (b) $\delta^{18}\text{O}_{\text{v-SMOW}}$ vs. MgO, and (c) ${}^{87}\text{Sr}/{}^{86}\text{Sr}$ vs. MgO. Strontium and oxygen isotopic data of the postcollisional UPVR and the Himalayan basement are from Zhao et al. (2009) and references therein. Isotopic compositions of geochemical end-members are listed in Table 4. Modeling crustal contamination hyperbolae with different ratios of mantle to crust (K) are shown.

and (iii) nearly flat HREE patterns displayed by early-Miocene zircons from the UPVR (Fig. 5b), suggesting garnet-present crystallization conditions (Liu et al., 2014). It is noteworthy that the UPVR zircons with low HREEs cannot crystallize from the highly HREE-depleted adakitic magmas because of zircons' very strong preference for HREEs. Therefore, considering zircons' magmatic origin

(high Th/U ratios; Fig. 5a), the melting residues after adakite melt extraction in the thickened lower crust is a possible source supplying very limited HREEs. Zircons crystallized from such incompletely extracted interstitial residual melt, which is highly depleted in HREEs, would have flat HREE pattern (Liu et al., 2014). However, this explanation requires that the adakitic magmatism occurred prior to the ultrapotassic magmatism. It can be supported by Xungba postcollisional magmatism because, in the Xungba basin, ultrapotassic lavas and underlying potassiac lavas with adakitic signatures form a "bimodal" volcanic sequence (Fig. 2).

The Mesozoic–Cenozoic magmatic zircons, with varying but overall positive $\epsilon_{\text{Hf}}(t)$ values, have also been found in the Tibetan ultrapotassic rocks, indicating contributions from juvenile crust produced during episodic oceanic subduction events and India–Asia convergence (Fig. 5c) (Sun et al., 2008; Chan et al., 2009; Liu et al., 2011b, 2014). Therefore, input from thickened lower crust that had been reworked by juvenile mantle input during Mesozoic–Cenozoic magmatism is required to explain the petrogenesis of the Tibetan ultrapotassic rocks.

6.1.3. Mantle metasomatism during Neo-Tethyan oceanic and/or Indian continental subduction

In southern Tibet, the most primitive UPVR, with MgO content up to 12 wt.% (Ding et al., 2006; Zhao et al., 2009), have higher Sr–O isotopic ratios than those most evolved ultrapotassic magma whose MgO content is close to 3 wt.% (Fig. 9b and c). This paradox can be explained by the metasomatism of the Tibetan mantle lithosphere prior to the assimilating crustal components mentioned above. The Fe-rich olivine and hydrous mineral phases (i.e., phlogopite) in the mantle xenoliths entrained by ultrapotassic magma also point to a metasomatized mantle source (Liu et al., 2011a). The mantle metasomatic event most likely occurred recently in response to recent Tethyan seafloor subduction and Indian lithosphere underthrusting, as is evidenced by the Mesozoic–Cenozoic magmatic zircon xenocrysts in the UPVR, which are consistent with outcropped magmatism genetically associated with the Neo-Tethyan seafloor subduction, slab rollback and break-off (Sun et al., 2008; Liu et al., 2014).

In Fig. 10, average upper, middle, and lower continental crust and partial melts derived from the ancient Lhasa basement have been shown for comparison. Crustal contamination cannot explain some trace element features of the UPVR because the continental crust contaminants would only dilute the enriched primitive melts (cf. Conticelli, 1998). Therefore, some incompatible element ratios (e.g., Th/Yb, Ba/La, Hf/Sr and Zr/Hf), which are largely immune to the crustal contamination, can be used as effective tracers for estimating mantle metasomatic agents (Fig. 10e and f) (Ben Othman et al., 1989; Dupuy et al., 1992; Ionov et al., 1993; Weyer et al., 2003; Prelević et al., 2012).

In the Th/Yb vs. Ba/La plot (Fig. 10e), ultrapotassic rocks in the Lhasa terrane display elevated Th/Yb with low and limited Ba/La. Because of the difference of element mobility in hydrous fluids (i.e., LILEs are more soluble

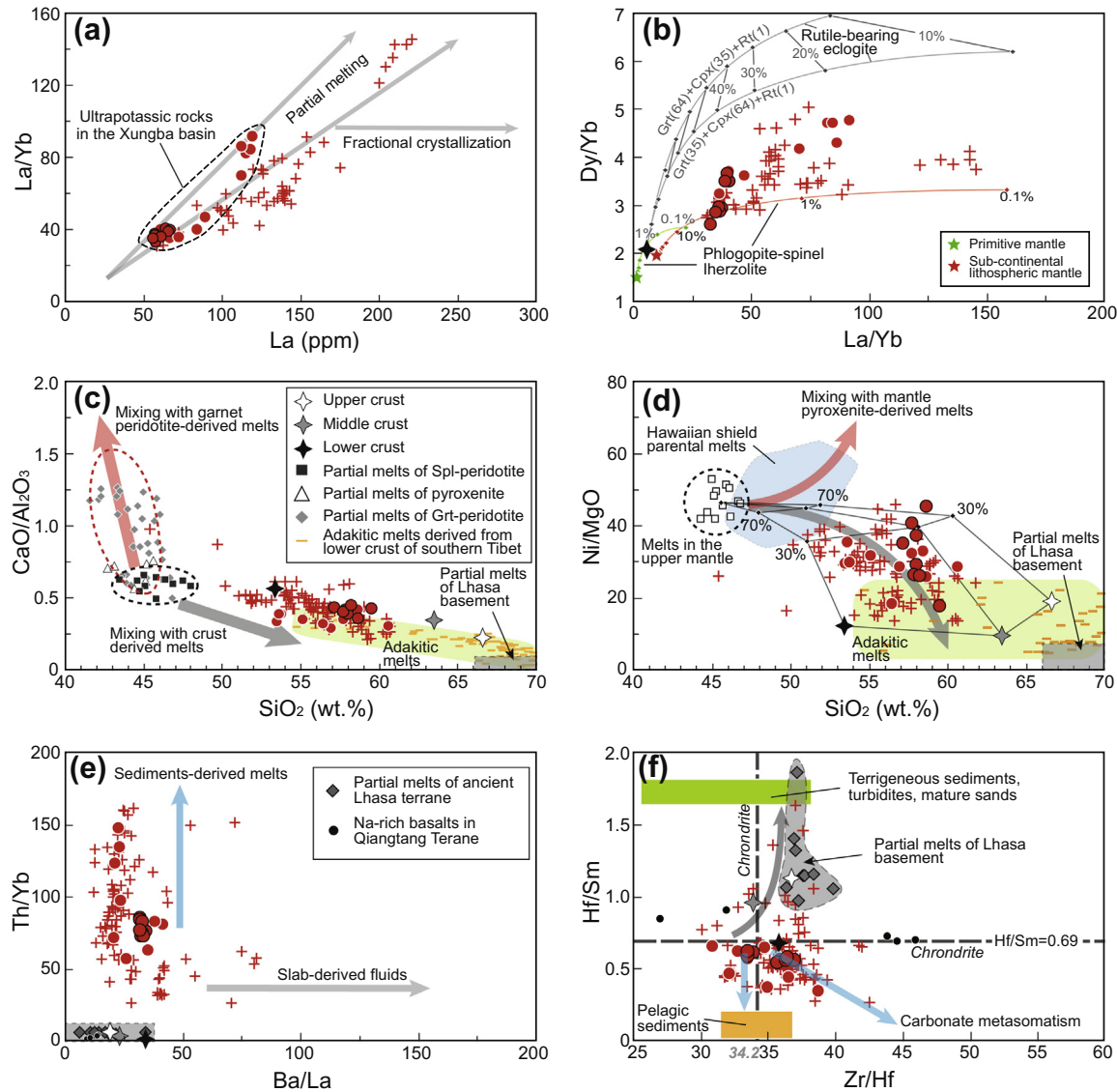


Fig. 10. Plots of (a) La/Yb vs. La and (b) Dy/Yb vs. La/Yb; data sources of the UPVR from the central Lhasa subterrane are from references in Fig. 1. Partial melting curves were calculated from batch melting equation. La, Dy, and Yb concentrations of primitive mantle and sub-continental lithospheric mantle are from Sun and McDonough (1989) and McDonough (1990), respectively. The mineralogy and partition coefficients of mantle and lower crust were listed in Table 5. (c) CaO/Al₂O₃ vs. SiO₂, data sources: melts derived from Spl-peridotite (Gaetani and Grove, 1998), Grt-peridotite (Herzberg and Zhang, 1996; Gaetani and Grove, 1998; Tennen et al., 2012), and mantle pyroxenite (Hirschmann et al., 2003); adakitic melts (see references in Fig. 1). (d) Ni/MgO vs. SiO₂; data sources: melts in the upper mantle are from Herzberg and Zhang (1996), Hawaiian shield parental melts are from Sobolev et al. (2005) and references therein. The compositions of upper, middle and lower crust are from Rudnick and Gao (2003). (e) Th/Yb vs. Ba/La, after Woodhead et al. (2001). Partial melts of ancient Lhasa basement are from Zhu et al. (2012a). (f) Hf/Sr vs. Zr/Hf, trace elements ratios for turbidite and pelagic sediments are from McLennan et al. (1990) and Ben Othman et al. (1989), respectively.

than HFSEs and REEs), the large Th/Yb (vertical) variation reflects source input from subducted sediments rather than slab-derived fluids (Woodhead et al., 2001). Additionally, considering the similar geochemical behavior among Zr, Hf, and Sm during partial melting (McDonough, 1990), Tibetan ultrapotassic rocks have fairly constant chondritic Zr/Hf ratios (30–40) with Hf/Sr ratios varying over a large range and deviating from the chondritic value for Hf/Sr (0.69) (Fig. 10f). The Hf/Sr ratios of continental crust components, terrigenous sediments, turbidites and mature sands, with high abundances of zircons, are

commonly super-chondritic (Fig. 10f) because zircon is Hf-enriched and LREE-depleted (Hoskin and Schaltegger, 2003; Prelević et al., 2012). The super-chondritic Hf/Sr ratios of some UPVR samples therefore may imply an additional input of zircon-rich sediments (e.g., terrigenous sediments, turbidites, mature sands) to the mantle source region or assimilating upper-middle continental crust components during magmatic ascent. However, many ultrapotassic samples, including the Xungba UPVR, display sub-chondritic Hf/Sr ratios and negative variation between Hf/Sr and Zr/Hf (Fig. 10f), suggesting other

metasomatic agents in the mantle sources. The pelagic sediments and marine pelite, which contain relatively few zircons, are characterized by much lower Hf/Sm ratios (Fig. 10f). Furthermore, the appearance of low Hf/Sm but high Zr/Hf ratios in some UPVR samples may reflect a mantle source region modified by carbonate-related metasomatism (Fig. 10f) (Dupuy et al., 1992; Ionov et al., 1993). Thus, the mantle sources of the UPVR in the Lhasa terrane may have also been enriched by pelagic sediments and marine carbonates derived from the Neo-Tethyan seafloor subduction. This interpretation is further supported by the high $(\text{La/Yb})_{\text{N}}$ but low Ti/Eu ratios displayed by clinopyroxenes in mantle xenoliths (Liu et al., 2011a), which points to carbonate-related mantle metasomatism (Coltorti et al., 1999).

Considering the underthrusting of Indian continental lithosphere following the Indian–Asia collision (cf. Freymueller, 2011), it is apparent that the Himalayan basement is a possible agent in metasomatizing the source region of ultrapotassic rocks (Ding et al., 2003; Zhao et al., 2009). However, both the Indian continent and central Lhasa subterrane are derived from the breakup and dispersal of Gondwanaland (Zhu et al., 2011b; Zhang et al., 2012) and have similar Sr–Nd–O isotopic compositions (Fig. 8a) (Vidal et al., 1982; Göpel et al., 1984; Zhu et al., 2013). Accordingly, it is difficult to distinguish Indian material inputs into mantle sources of UPVR from the influence of crustal contamination of ancient Lhasa basement. If the spatial distribution of the ultrapotassic magmatism and the compositional differences between the central (ancient) and northern/southern (juvenile) subterranea are considered, we can find that the Tibetan mantle lithosphere metasomatism may have more complex histories and the recent metasomatized lithosphere is only one end-member controlling the geochemical signatures of the UPVR (Williams et al., 2004; Zhao et al., 2009; Guo et al., 2013).

In summary, postcollisional ultrapotassic rocks in the Xungba basin as well as those from the entire Lhasa terrane were derived from a phlogopite-bearing spinel peridotite source, which had been metasomatized during previous Tethyan oceanic subduction, and then mixed with melts derived from thickened lower crust (eclogite-facies or garnet-bearing granulite facies) and ancient Lhasa basement (middle or upper crust) during magmatic ascent. More work is needed to distinguish the Indian input into the mantle sources of ultrapotassic rocks, if this process did exist during continental convergence, from crustal contamination of the central Lhasa subterrane crust.

6.2. Petrogenesis of adakitic potassic volcanic rocks (Group 2)

In the Sr–Nd isotopic array (Fig. 8a), Xungba potassic volcanic rocks (Group 2) show higher Sr initial isotopic ratios relative to the overlying UPVR and coeval potassic magmatism in the central Lhasa subterrane (Chen et al., 2010, 2011). Compared with the Xungba UPVR, the PVR have lower incompatible elements (e.g., Th, U, Sr, Ba; Fig. 7b) and distinct Sr–Nd isotopes, ruling out an origin by fractional crystallization from the mantle-derived

ultrapotassic magmas. Furthermore, the high SiO₂, low MgO and compatible elements (e.g., Cr, Ni) concentrations also indicate that the Xungba PVR were derived from crustal sources rather than a mantle source (Table 2).

Despite the similarities in Sr–Nd–O isotopic compositions, the Xungba PVR could not have formed by partial melting of subducted Indian continent for two reasons: (i) their Pb isotopic compositions resemble the Lhasa basement rather than the Himalayan basement (Gariépy et al., 1985; Liao, 2003), and (ii) the PVR have low MgO and compatible elements abundances (Cr = 32–129 ppm, Ni = 4–74 ppm), which is inconsistent with melts derived from subducted continental crust since this kind of melt will inevitably react with the mantle wedge and acquire excess compatible elements. The crustal contamination trend between $\delta^{18}\text{O}_{\text{V-SMOW}}$ and $^{87}\text{Sr}/^{86}\text{Sr}$ and negative correlations between Sr–O isotopic ratios and MgO confirm that the evolved isotopic compositions of the PVR are due to assimilation of ancient Lhasa basement (Fig. 9b and c).

In discrimination diagrams (Fig. 11a and b) (Defant and Drummond, 1990; Richards and Kerrich, 2007), except for a few samples with lower Sr/Y ratios, most Xungba PVR have adakitic geochemical signatures with high Sr/Y and La/Yb ratios but low Y and Yb abundances. However, the negative Sr and Eu anomalies observed in the PVR suggest that the Group II rocks are not typical “adakite”. Aside from melting a subducted young oceanic crust, an adakitic signature can be achieved through: (i) fractional crystallization of clinopyroxene that is selectively enriched in HREEs (Castillo et al., 1999; Richards and Kerrich, 2007); (ii) partial melting of high Sr/Y sources under low pressure conditions (cf. Moyen, 2009); and (iii) melting of thickened lower crust under eclogite-facies conditions (cf. Chung et al., 2009). In the case of the Xungba PVR, no fractionation trends of pyroxene and amphibole can be found in the Rb/Sr–Sr diagrams (Fig. 11c), precluding the adakitic signature from fractional crystallization of HREE-rich minerals. The adakite-like signature of the PVR could not have originated from high-Sr/Y sources, as the Sr/Y ratio of gabbro xenolith entrained by ultrapotassic magma is as low as 32.8 (Miller et al., 1999), slightly higher than that of average lower crust (Sr/Y = 21.8, Rudnick and Gao, 2003). If we consider the compressional regime during the Eocene (Chung et al., 2005), the Xungba PVR is best interpreted as resulting from partial melting of thickened lower crust. However, in comparison with typical adakitic melts (Richards and Kerrich, 2007; Castillo, 2012), the PVR are marked by a weak negative Eu anomaly in general and a few PVR samples have relatively low Sr/Y ratios and strong negative Eu anomalies (Fig. 11a and d). These differences can be reconciled with the existence of plagioclase fractional crystallization. As illustrated in Fig. 11a, a rapid decreasing trend in Sr/Y ratios with plagioclase fractionation can be modeled by assuming the parent adakitic magma containing 1000 ppm of Sr and 12 ppm of Y. The plagioclase fractionation trend shown in mineral vector diagram (Fig. 11c) and the positive correlation trend between Eu/Eu^{*} and Sr (Fig. 11d) are consistent with fractional crystallization of plagioclase in the petrogenesis of the PVR. Therefore, the Xungba PVR with adakitic

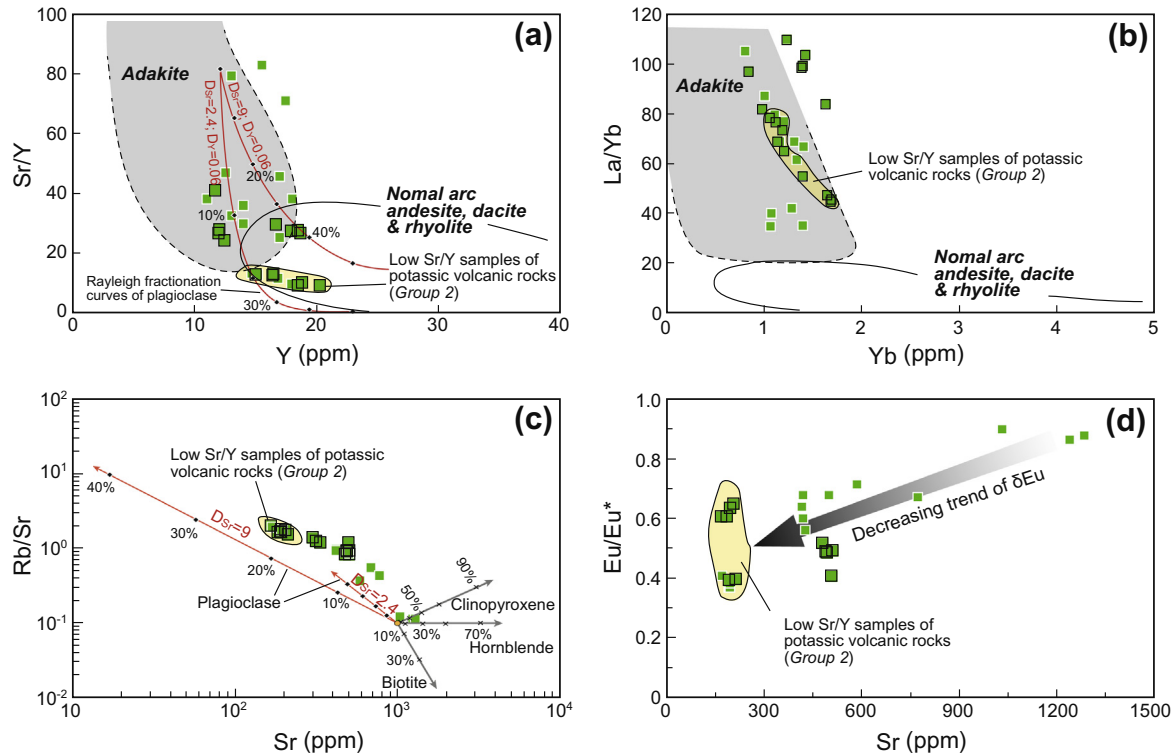


Fig. 11. Plots of the Xungba potassic rocks (Group 2). (a) Sr/Y vs. Y, Adakite, normal arc andesite, dacite & rhyolite are from Defant and Drummond (1990). (b) La/Yb vs. Yb, discrimination lines are from Richards and Kerrich (2007) and Castillo (2012). (c) Mineral vector diagram and (d) Eu/Eu* vs. Sr diagram, both of which indicate the effects of plagioclase fractional crystallization. The plagioclase fractionation curves with different strontium partition coefficients in (a) and the vectors of plagioclase in (c) are calculated with 10% intervals. These trace elements modeling are calculated from Rayleigh fractionation equation with the initial concentrations of Rb, Sr and Y taken as 100, 1000 and 12 ppm, respectively.

geochemical signatures were derived from thickened lower crust and modified by crustal contamination with ancient Lhasa basement and by fractional crystallization of plagioclase.

6.3. Geodynamic implications

Although the exact timing and processes of plateau uplift remain in dispute, postcollisional magmatism and geologic episodes, including accelerated uplift of southern Tibet (Harrison et al., 1992; Yin and Harrison, 2000), changes in crustal stress state and deformation style (Blisniuk et al., 2001; Kapp et al., 2008; Mitsuishi et al., 2012), high rates of denudation and sedimentation (Clift and Gaedicke, 2002; Uddin and Lundberg, 2004; Carter et al., 2010; Enkelmann et al., 2011; Kirstein, 2011), rapid increase of the $^{87}\text{Sr}/^{86}\text{Sr}$ ratio in seawater (DePaolo and Ingram, 1985; Krishnaswami et al., 1992) and the transformation of global climate system from zonal to a monsoonal pattern (Guo et al., 2008), all appear to have taken place simultaneously in the early Miocene (Fig. 12). Therefore, as the earliest magmatic record, the “bimodal” volcanic sequences formed by early-Miocene ultrapotassic lavas and underlying potassic lavas in Xungba basin may symbolize the onset of geodynamic processes in southern Tibet

during postcollisional stage and point to an extensional tectonic regime.

However, the synchronous adakitic magmatism and the petrogenetic relationship between Tibetan ultrapotassic rocks and eclogite-facies lower crust require a thickened lower crust for postcollisional magmatism. An effective geodynamic model should be able to reconcile the “paradox” between extentional tectonic regime and the overthickened crust, and to accommodate northward underthrusting of the Indian lithosphere with the existence of thickened Tibetan lower crust. A possible scenario is that the lower part of overthickened lithospheric mantle was delaminated, which may have triggered postcollisional magmatism and surface uplift and extension in the southern Tibet as suggested by previously (Chung et al., 2005; Zhao et al., 2009). In this scenario, with continued northward underthrusting of Indian continental lithosphere, the rheologically heterogeneous lithospheric mantle would become overthickened. Because of the gravitational instability and mantle convection, the delamination started from the northern front of the overthickened lithospheric mantle and was gradually replaced by hotter asthenosphere. Consequently, the upwelling of the asthenosphere resulted in partial melting of the residual part of lithospheric mantle metasomatized during Mesozoic–Cenozoic Neo-Tethyan seafloor

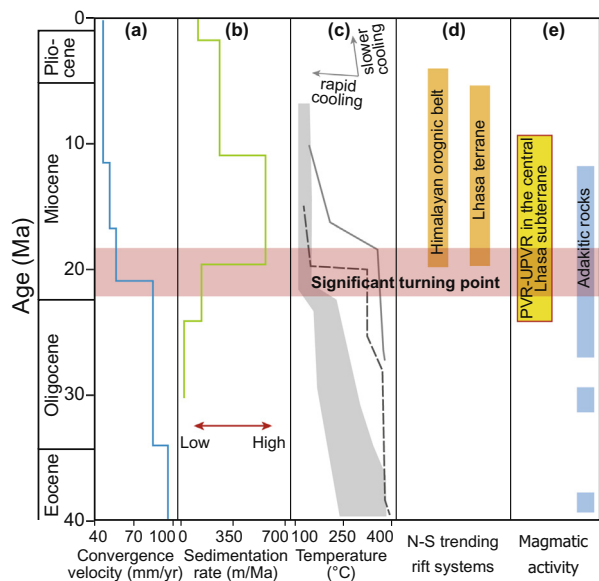


Fig. 12. Correlation of magmatic, tectonic and geomorphic events from Eocene to Pliocene in southern Tibet: (a) the India–Asia convergence rate is from van Hinsbergen et al. (2011); (b) sedimentation rate in the peripheral basins of the Tibet Plateau is from Clift and Gaedicke (2002); (c) thermal evolution history of Gangdese batholith and Kailas conglomerate are from Harrison et al. (1993), Copeland et al. (1995) and Kirstein (2011); (d) the onset of N–S trending rifts are base on Blisniuk et al. (2001), Kapp et al. (2008), and Mitsuishi et al. (2012); (e) magmatic age data, see references in Fig. 1.

subduction and thickened lower crust, generating the ultrapotassic and potassiac volcanism in the central Lhasa subterrane, respectively. The poloidal mantle flow around the delaminated mantle lithosphere may be responsible for the accelerated uplift of southern Tibet from about 20 Ma. Note that, in this dynamic model, the delaminating front of the mantle lithosphere may be recorded in the post-collisional magmatism in time and space in the Lhasa terrane (Fig. 1a).

7. CONCLUSIONS

- (1) The postcollisional volcanic sequences in the Xungba basin consist of ultrapotassiac (UPVR) and potassiac volcanic rocks (PVR) that erupted coevally at ~23 Ma.
- (2) The UPVR resulted from partial melting of hydrous mantle lithosphere under spinel facies conditions. The mantle lithosphere has experienced multiple metasomatic events during the Neo-Tethyan seafloor subduction. The thickened lower crust and ancient Lhasa basement rocks have both contributed to the Tibetan ultrapotassiac magmatism.
- (3) The PVR with adakitic signature resulted from melting of the thickened lower crust with the melt contaminated by ancient Lhasa basement rocks during

ascent. Plagioclase crystallization is responsible for the low Sr/Y and high Y for some of the PVR samples, but has little effect on the La/Yb and Yb.

- (4) The extensional tectonic regime and the thickened crust together make the UPVR and PVR magmatism possible, and the UPVR and PVR rocks offer prime opportunities to discuss deep processes in the early Miocene. Delamination of lower part of the overthickened mantle lithosphere is a possible scenario to explain the plateau uplift, surface extension and the close relationship between postcollisional magmatism and thickened lower crust.

ACKNOWLEDGEMENTS

The work was supported by the National Key Project for Basic Research (2011CB403102), NSF of China (Grants 41273044, 40873023, 41225006), NSF of U.S. (Grants EAR1111959, 1111586), CGS-1212011121260, Sinoprobe-04-02, IRT1083, 111 Program (B07011), and IGCP/SIDA-600. We appreciate three anonymous reviewers for constructive comments and Editors Marc Norman and Weidong Sun for handling the manuscript. We thank Yongsheng Liu, Zhaochu Hu and Honglin Yuan for assistance in the zircon analysis, and Shihong Tian in whole rock oxygen isotope analysis.

APPENDIX A. SUPPLEMENTARY DATA

Supplementary data associated with this article can be found, in the online version, at <http://dx.doi.org/10.1016/j.gca.2014.03.031>.

REFERENCES

- Aikman A. B., Harrison T. M. and Ding L. (2008) Evidence for early (≥ 44 Ma) Himalayan crustal thickening, Tethyan Himalaya, southeastern Tibet. *Earth Planet. Sci. Lett.* **274**, 14–23.
- Aikman A. B., Harrison T. M. and Herman J. (2012) The origin of Eo- and Neohimalayan granitoids, Eastern Tibet. *J. Asian Earth Sci.* **58**, 143–157.
- Andersen T. (2002) Correction of common lead in U–Pb analyses that do not report ^{204}Pb . *Chem. Geol.* **192**, 59–79.
- Avanzinelli R., Lustrino M., Mattei M., Melluso L. and Conticelli S. (2009) Potassiac and ultrapotassiac magmatism in the circum-Tyrrhenian region: significance of carbonated pelitic vs. pelitic sediment recycling at destructive plate margins. *Lithos* **113**, 213–227.
- Belousova E., Griffin W., O’Reilly S. Y. and Fisher N. (2002) Igneous zircon: trace element composition as an indicator of source rock type. *Contrib. Miner. Petrol.* **143**, 602–622.
- Ben Othman D., White W. M. and Patchett J. (1989) The geochemistry of marine sediments, island arc magma genesis, and crust–mantle recycling. *Earth Planet. Sci. Lett.* **94**, 1–21.
- Blisniuk P. M., Hacker B. R., Glodny J., Ratschbacher L., Bi S., Wu Z., McWilliams M. O. and Calvert A. (2001) Normal faulting in central Tibet since at least 13.5 Myr ago. *Nature* **412**, 628–632.
- Bouilhol P., Jagoutz O., Hanchar J. M. and Dudas F. O. (2013) Dating the India–Eurasia collision through arc magmatic records. *Earth Planet. Sci. Lett.* **366**, 163–175.

- Boynton W. V. (1984) Geochemistry of the rare earth elements: meteorite studies. In *Rare Earth Element Geochemistry* (ed. P. Henderson). Elsevier, Amsterdam, pp. 63–114.
- Carter A., Najman Y., Bahroodi A., Bown P., Garzanti E. and Lawrence R. D. (2010) Locating earliest records of orogenesis in western Himalaya: evidence from paleogene sediments in the Iranian Makran region and Pakistan Katawaz basin. *Geology* **38**, 807–810.
- Castillo P. R., Janney P. E. and Solidum R. U. (1999) Petrology and geochemistry of Camiguin Island, southern Philippines: insights to the source of adakites and other lavas in a complex arc setting. *Contrib. Miner. Petrol.* **134**, 33–51.
- Castillo P. R. (2012) Adakite petrogenesis. *Lithos* **134–135**, 304–316.
- Chan G. H. N., Waters D. J., Searle M. P., Aitchison J. C., Horstwood M. S. A., Crowley Q., Lo C. H. and Chan J. S. L. (2009) Probing the basement of southern Tibet: evidence from crustal xenoliths entrained in a Miocene ultrapotassic dyke. *J. Geol. Soc. London* **166**, 45–52.
- Chen J. L., Xu J. F., Wang B. D., Kang Z. Q. and Li J. (2010) Origin of cenozoic alkaline potassiac volcanic rocks at KonglongXiang, Lhasa terrane, Tibetan Plateau: products of partial melting of a mafic lower-crustal source? *Chem. Geol.* **273**, 286–299.
- Chen J. L., Xu J. F., Zhao W. X., Dong Y. H., Wang B. D. and Kang Z. Q. (2011) Geochemical variations in Miocene adakitic rocks from the western and eastern Lhasa terrane: implications for lower crustal flow beneath the Southern Tibetan Plateau. *Lithos* **125**, 928–939.
- Chen J. L., Zhao W. X., Xu J. F., Wang B. D. and Kang Z. Q. (2012) Geochemistry of Miocene trachytes in Bugasi, Lhasa block, Tibetan Plateau: mixing products between mantle-and crust-derived melts? *Gondwana Res.* **21**, 112–122.
- Chu M. F., Chung S. L., Song B., Liu D., O'Reilly S. Y., Pearson N. J., Ji J. and Wen D. J. (2006) Zircon U-Pb and Hf isotope constraints on the Mesozoic tectonics and crustal evolution of southern Tibet. *Geology* **34**, 745–848.
- Chu M. F., Chung S. L., O'Reilly S. Y., Pearson N. J., Wu F. Y., Li X. H., Liu D., Ji J., Chu C. H. and Lee H. Y. (2011) India's hidden inputs to Tibetan orogeny revealed by Hf isotopes of Transhimalayan zircons and host rocks, *Earth Planet. Sci. Lett.* **307**, 479–486.
- Chung S. L., Chu M. F., Zhang Y., Xie Y., Lo C. H., Lee T. Y., Lan C. Y., Li X., Zhang Q. and Wang Y. (2005) Tibetan tectonic evolution inferred from spatial and temporal variations in post-collisional magmatism. *Earth Sci. Rev.* **68**, 173–196.
- Chung S. L., Chu M. F., Ji J., O'Reilly S. Y., Pearson N. J., Liu D., Lee T. Y. and Lo C. H. (2009) The nature and timing of crustal thickening in Southern Tibet: geochemical and zircon Hf isotopic constraints from postcollisional adakites. *Tectonophysics* **477**, 36–48.
- Clift P. and Gaedicke C. (2002) Accelerated mass flux to the Arabian Sea during the middle to late Miocene. *Geology* **30**, 207–210.
- Coltorti M., Bonadiman C., Hinton R., Siena F. and Upton B. (1999) Carbonatite metasomatism of the oceanic upper mantle: evidence from clinopyroxenes and glasses in ultramafic xenoliths of Grande Comore, Indian Ocean. *J. Petrol.* **40**, 133–165.
- Conticelli S. (1998) The effect of crustal contamination on ultrapotassic magmas with lamproitic affinity: mineralogical, geochemical and isotope data from the Torre Alfina lavas and xenoliths, Central Italy. *Chem. Geol.* **149**, 51–81.
- Conticelli S., Guarneri L., Farinelli A., Mattei M., Avanzinelli R., Bianchini G., Boari E., Tommasini S., Tiepolo M. and Prelevic D. (2009a) Trace elements and Sr-Nd-Pb isotopes of K-rich, shoshonitic, and calc-alkaline magmatism of the Western Mediterranean region: genesis of ultrapotassic to calc-alkaline magmatic associations in a post-collisional geodynamic setting. *Lithos* **107**, 68–92.
- Conticelli S., Marchionni S., Rosa D., Giordano G., Boari E. and Avanzinelli R. (2009b) Shoshonite and sub-alkaline magmas from an ultrapotassic volcano: Sr-Nd-Pb isotope data on the Roccamonfina volcanic rocks, Roman Magmatic Province, Southern Italy. *Contrib. Miner. Petrol.* **157**, 41–63.
- Copeland P., Harrison T. M., Yun P., Kidd W. S. F., Roden M. and Zhang Y. (1995) Thermal evolution of the Gangdese batholith, southern Tibet: a history of episodic unroofing. *Tectonics* **14**, 223–236.
- Corfu F., Hanchar J. M., Hoskin P. W. O. and Kinny P. (2003) Atlas of zircon textures. *Rev. Mineral. Geochem.* **53**, 469–500.
- Coulon C., Maluski H., Bollinger C. and Wang S. (1986) Mesozoic and Cenozoic volcanic rocks from central and southern Tibet: ^{39}Ar - ^{40}Ar dating, petrological characteristics and geodynamical significance. *Earth Planet. Sci. Lett.* **79**, 281–302.
- DeBon F., Fort P. L. E., Sheppard S. M. F. and Sonet J. (1986) The four plutonic belts of the Transhimalaya-Himalaya: a chemical, mineralogical, isotopic, and chronological synthesis along a Tibet-Nepal section. *J. Petrol.* **27**, 219–250.
- Defant M. J. and Drummond M. S. (1990) Derivation of some modern arc magmas by melting of young subducted lithosphere. *Nature* **347**, 662–665.
- DePaolo D. J. and Ingram B. L. (1985) High-resolution stratigraphy with strontium isotopes. *Science* **227**, 938–941.
- Dewey J. F., Shackleton R. M., Chang C. F. and Sun Y. (1988) The tectonic evolution of the Tibetan Plateau. *Philos. Trans. R. Soc. Lond.* **A327**, 379–413.
- Ding L., Kapp P., Zhong D. and Deng W. (2003) Cenozoic volcanism in Tibet: evidence for a transition from oceanic to continental subduction. *J. Petrol.* **44**, 1833–1865.
- Ding L., Yue Y., Cai F., Xu X., Zhang Q. and Lai Q. (2006) ^{40}Ar / ^{39}Ar Geochronology, geochemical and Sr-Nd-O isotopic characteristics of the high-Mg ultrapotassic rocks in Lhasa block of Tibet: implications in onset time and depth of NS-striking rift system. *Acta Geol. Sinica* **80**, 1252–1261.
- Dong X., Zhang Z. and Santosh M. (2010) Zircon U-Pb chronology of the Nyingtri Group, Southern Lhasa Terrane, Tibetan Plateau: implications for Grenvillian and Pan-African Provenance and Mesozoic-Cenozoic metamorphism. *J. Geol.* **118**, 677–690.
- Dupuy C., Liotard J. M. and Dostal J. (1992) Zr/Hf fractionation in intraplate basaltic rocks: carbonate metasomatism in the mantle source. *Geochim. Cosmochim. Acta* **56**, 2417–2423.
- Enkelmann E., Ehlers T. A., Zeitler P. K. and Hallet B. (2011) Denudation of the Namche Barwa antiform, eastern Himalaya. *Earth Planet. Sci. Lett.* **307**, 323–333.
- Freymueller J. T. (2011) Earth science. A new mechanical model for Tibet. *Nature* **472**, 48–49.
- Göpel C., Allegre C. J. and Xu R. H. (1984) Lead isotopic study of the Xigaze ophiolite (Tibet): the problem of the relationship between magmatites (gabbros, dolerites, lavas) and tectonites (harzburgites). *Earth Planet. Sci. Lett.* **69**, 301–310.
- Gaetani G. A. and Grove T. L. (1998) The influence of water on melting of mantle peridotite. *Contrib. Miner. Petrol.* **131**, 323–346.
- Gao Y., Hou Z., Kamber B. S., Wei R., Meng X. and Zhao R. (2007) Lamproitic rocks from a continental collision zone: evidence for recycling of subducted Tethyan Oceanic sediments in the mantle beneath southern Tibet. *J. Petrol.* **48**, 729–752.
- Gao Y., Wei R., Ma P., Hou Z. and Yang Z. (2009) Post-collisional ultrapotassic volcanism in the Tangra Yumco-Xurucu graben, south Tibet: constraints from geochemistry and Sr-Nd-Pb isotope. *Lithos* **110**, 129–139.

- Gariépy C., Allègre C. J. and Xu R. H. (1985) The Pb-isotope geochemistry of granitoids from the Himalaya–Tibet collision zone: implications for crustal evolution. *Earth Planet. Sci. Lett.* **74**, 220–234.
- Grégoire M., Moine B., O'Reilly S. Y., Cottin J. and Giret A. (2000) Trace element residence and partitioning in mantle xenoliths metasomatized by highly alkaline, silicate-and carbonate-rich melts (Kerguelen Islands, Indian Ocean). *J. Petrol.* **41**, 477–509.
- Green T. H., Blundy J. D., Adam J. and Yaxley G. M. (2000) SIMS determination of trace element partition coefficients between garnet, clinopyroxene and hydrous basaltic liquids at 2–7.5 GPa and 1080–1200 °C. *Lithos* **53**, 165–187.
- Guan Q., Zhu D. C., Zhao Z. D., Dong G. C., Zhang L. L., Li X. W., Liu M., Mo X. X., Liu Y. S. and Yuan H. L. (2012) Crustal thickening prior to 38 Ma in southern Tibet: evidence from lower crust-derived adakitic magmatism in the Gangdese Batholith. *Gondwana Res.* **21**, 88–99.
- Guo Z., Wilson M., Liu J. and Mao Q. (2006) Post-collisional, potassic and ultrapotassic magmatism of the northern Tibetan Plateau: constraints on characteristics of the mantle source, geodynamic setting and uplift mechanisms. *J. Petrol.* **47**, 1177–1220.
- Guo Z., Wilson M. and Liu J. (2007) Post-collisional adakites in south Tibet: products of partial melting of subduction-modified lower crust. *Lithos* **96**, 205–224.
- Guo Z. T., Sun B., Zhang Z. S., Peng S. Z., Xiao G. Q., Ge J. Y., Hao Q. Z., Qiao Y. S., Liang M. Y. and Liu J. F. (2008) A major reorganization of Asian climate by the early Miocene. *Clim. Past* **4**, 153–174.
- Guo Z. and Wilson M. (2012) The Himalayan leucogranites: constraints on the nature of their crustal source region and geodynamic setting. *Gondwana Res.* **22**, 360–376.
- Guo Z., Wilson M., Zhang M., Cheng Z. and Zhang L. (2013) Post-collisional, K-rich mafic magmatism in south Tibet: constraints on Indian slab-to-wedge transport processes and plateau uplift. *Contrib. Miner. Petrol.* **165**, 1311–1340.
- Harrison T. M., Copeland P., Kidd W. S. F. and Yin A. (1992) Raising Tibet. *Science* **255**, 1663–1670.
- Harrison T. M., Copeland P., Hall S. A., Quade J., Burner S., Ojha T. P. and Kidd W. S. F. (1993) Isotopic preservation of Himalayan/Tibetan uplift, denudation, and climatic histories of two molasse deposits. *J. Geol.* **101**, 157–175.
- Harrison T. M., Lovera O. M. and Grove M. (1997) New insights into the origin of two contrasting Himalayan granite belts. *Geology* **25**, 899–902.
- Harrison T. M., Yin A., Grove M., Lovera O. M. and Ryerson F. J. (2000) The Zedong Window: a record of superposed Tertiary convergence in southeastern Tibet. *J. Geophys. Res.* **105**, 19211–19230.
- Hébert R., Guilmette C., Dostal J., Bezard R., Lesage G., Bédard É. and Wang C. (2014) Miocene post-collisional shoshonites and their crustal xenoliths, Yarlung Zangbo Suture Zone southern Tibet: geodynamic implications. *Gondwana Res.* **25**, 1263–1271.
- Herzberg C. and Zhang J. (1996) Melting experiments on anhydrous peridotite KLB-1: compositions of magmas in the upper mantle and transition zone. *J. Geophys. Res.* **101**, 8271–8295.
- Hirschmann M. M. and Stolper E. M. (1996) A possible role for garnet pyroxenite in the origin of the “garnet signature” in MORB. *Contrib. Miner. Petrol.* **124**, 185–208.
- Hirschmann M. M., Kogiso T., Baker M. B. and Stolper E. M. (2003) Alkaline magmas generated by partial melting of garnet pyroxenite. *Geology* **31**, 481–484.
- Hoskin P. W. O. and Schaltegger U. (2003) The composition of zircon and igneous and metamorphic petrogenesis. *Rev. Mineral. Geochem.* **53**, 27–62.
- Hou Z. Q., Gao Y. F., Qu X. M., Rui Z. Y. and Mo X. X. (2004) Origin of adakitic intrusives generated during mid-Miocene east–west extension in southern Tibet. *Earth Planet. Sci. Lett.* **220**, 139–155.
- Hou Z. Q., Zheng Y. C., Zeng L. S., Gao L. E., Huang K. X., Li W., Li Q. Y., Fu Q., Liang W. and Sun Q. Z. (2012) Eocene–Oligocene granitoids in southern Tibet: constraints on crustal anatexis and tectonic evolution of the Himalayan orogen. *Earth Planet. Sci. Lett.* **349–350**, 38–52.
- Ionov D. A., Dupuy C., O'Reilly S. Y., Kopylova M. G. and Genshaft Y. S. (1993) Carbonated peridotite xenoliths from Spitsbergen: implications for trace element signature of mantle carbonate metasomatism. *Earth Planet. Sci. Lett.* **119**, 283–297.
- Ji W. Q., Wu F. Y., Chung S. L., Li J. X. and Liu C. Z. (2009) Zircon U–Pb geochronology and Hf isotopic constraints on petrogenesis of the Gangdese batholith, southern Tibet. *Chem. Geol.* **262**, 229–245.
- Kang Z. Q., Xu J. F., Dong Y. H. and Wang B. D. (2008) Cretaceous volcanic rocks of Zenong Group in north-middle Lhasa block: products of southward subducting of the Slainajap Ocean? *Acta Petrol. Sin.* **24**, 303–314.
- Kapp J. L. D., Harrison T. M., Kapp P., Grove M., Lovera O. M. and Ding L. (2005) Nyainqntanglha Shan: a window into the tectonic, thermal, and geochemical evolution of the Lhasa block, southern Tibet. *J. Geophys. Res.* **110**. <http://dx.doi.org/10.1029/2004JB003330> (B08413).
- Kapp P., Taylor M., Stockli D. F. and Ding L. (2008) Development of active low-angle normal fault systems during orogenic collapse: insight from Tibet. *Geology* **36**, 7–10.
- Keshav S., Gudfinnsson G. H., Sen G. and Fei Y. (2004) High-pressure melting experiments on garnet clinopyroxenite and the alkalic to tholeiitic transition in ocean-island basalts. *Earth Planet. Sci. Lett.* **223**, 365–379.
- Kirstein L. A. (2011) Thermal evolution and exhumation of the Ladakh Batholith, northwest Himalaya, India. *Tectonophysics* **503**, 222–233.
- Kogiso T., Hirschmann M. M. and Frost D. J. (2003) High-pressure partial melting of garnet pyroxenite: possible mafic lithologies in the source of ocean island basalts. *Earth Planet. Sci. Lett.* **216**, 603–617.
- Kosarev G., King R., Sobolev S. V., Yuan X., Hanka W. and Oreshin S. (1999) Seismic evidence for a detached Indian lithospheric mantle beneath Tibet. *Science* **283**, 1306–1309.
- Krishnaswami S., Trivedi J. R., Sarin M. M., Ramesh R. and Sharma K. K. (1992) Strontium isotopes and rubidium in the Ganga–Brahmaputra river system: weathering in the Himalaya, fluxes to the Bay of Bengal and contributions to the evolution of oceanic $^{87}\text{Sr}/^{86}\text{Sr}$. *Earth Planet. Sci. Lett.* **109**, 243–253.
- Le Maitre R. W., Streckeisen A., Zanettin B., Le Bas M. J., Bonin B. and Bateman P. (2005) *Igneous Rocks: A Classification and Glossary of Terms*. Cambridge University Press, Cambridge, UK.
- Lee C. T. A., Harbert A. and Leeman W. P. (2007) Extension of lattice strain theory to mineral/mineral rare-earth element partitioning: an approach for assessing disequilibrium and developing internally consistent partition coefficients between olivine, orthopyroxene, clinopyroxene and basaltic melt. *Geochim. Cosmochim. Acta* **71**, 481–496.
- Lee H. Y., Chung S. L., Lo C. H., Ji J., Lee T. Y., Qian Q. and Zhang Q. (2009) Eocene Neotethyan slab breakoff in southern Tibet inferred from the Linzizong volcanic record. *Tectonophysics* **477**, 20–35.

- Lee H. Y., Chung S. L., Ji J., Qian Q., Gallet S., Lo C. H., Lee T. Y. and Zhang Q. (2012) Geochemical and Sr–Nd isotopic constraints on the genesis of the Cenozoic Linzizong volcanic successions, southern Tibet. *J. Asian Earth Sci.* **53**, 96–144.
- Liao Z. L. (2003) Peraluminous granites in southern Tibet: characteristics, genesis and tectonic implications. Ph.D. dissertation, School of Earth Science and Mineral Resources, China University of Geosciences, Beijing.
- Liu Y., Gao S., Yuan H., Zhou L., Liu X., Wang X., Hu Z. and Wang L. (2004) U–Pb zircon ages and Nd, Sr, and Pb isotopes of lower crustal xenoliths from North China Craton: insights on evolution of lower continental crust. *Chem. Geol.* **211**, 87–109.
- Liu Q. S., Jiang W., Jian P., Ye P. S., Wu Z. H. and Hu D. G. (2006) The zircon SHRIMP U–Pb age and petrochemical and geochemical features of Mesozoic muscovite monzogranite at Ningzhong, Tibet. *Acta Petrol. Sin.* **22**, 643–652.
- Liu Y. S., Hu Z. C., Gao S., Günther D., Xu J., Gao C. G. and Chen H. H. (2008) In situ analysis of major and trace elements of anhydrous minerals by LA-ICP-MS without applying an internal standard. *Chem. Geol.* **257**, 34–43.
- Liu Y. S., Gao S., Hu Z. C., Gao C. G., Zong K. Q. and Wang D. B. (2010) Continental and oceanic crust recycling-induced melt–peridotite interactions in the trans-North China Orogen: U–Pb dating, Hf isotopes and trace elements in zircons from mantle xenoliths. *J. Petrol.* **51**, 537–571.
- Liu C. Z., Wu F. Y., Chung S. L. and Zhao Z. D. (2011a) Fragments of hot and metasomatized mantle lithosphere in middle Miocene ultrapotassic lavas, southern Tibet. *Geology* **39**, 923–926.
- Liu D., Zhao Z. D., Zhu D. C., Wang Q., Sui Q. L., Liu Y. S., Hu Z. C. and Mo X. X. (2011b) The petrogenesis of post-collisional potassio–ultrapotassic rocks in Xungba basin, western Lhasa terrane: constraints from zircon U–Pb geochronology and geochemistry. *Acta Petrol. Sin.* **27**, 2045–2059.
- Liu D., Zhao Z. D., Zhu D. C., Niu Y., Liu S. A., Wang Q., Liu Y. S. and Hu Z. C. (2013) Zircon records from Miocene ultrapotassic rocks from southern Lhasa sub-terrane, Tibetan Plateau. *Acta Petrol. Sin.* **29**, 3703–3715.
- Liu D., Zhao Z., Zhu D. C., Niu Y. and Harrison T. M. (2014) Zircon xenocrysts in Tibetan ultrapotassic magmas: imaging the deep crust through time. *Geology* **42**, 43–46.
- Ludwig K. R. (2003) *Isoplot/Ex Version 3.00: A Geochronological Toolkit for Microsoft Excel*. Berkeley Geochronology Center, Berkeley, CA, USA..
- Macpherson C. G., Gamble J. A. and Matthey D. P. (1998) Oxygen isotope geochemistry of lavas from an oceanic to continental arc transition, Kermadec–Hikurangi margin, SW Pacific. *Earth Planet. Sci. Lett.* **160**, 609–621.
- Mahoney J. J., Frei R., Tejada M. L. G., Mo X. X., Leat P. T. and Nägler T. F. (1998) Tracing the Indian ocean mantle domain through time: isotopic results from old West Indian, East Tethyan, and South Pacific seafloor. *J. Petrol.* **39**, 1285–1306.
- McDade P., Blundy J. D. and Wood B. J. (2003) Trace element partitioning on the Tinaquillo Lherzolite solidus at 1.5 GPa. *Phys. Earth Planet. Inter.* **139**, 129–147.
- McDonough W. F. (1990) Constraints on the composition of the continental lithospheric mantle. *Earth Planet. Sci. Lett.* **101**, 1–18.
- McLennan S., Taylor S., McCulloch M. and Maynard J. (1990) Geochemical and Nd–Sr isotopic composition of deep-sea turbidites: crustal evolution and plate tectonic associations. *Geochim. Cosmochim. Acta* **54**, 2015–2050.
- Miller C., Schuster R., Klitzli U., Frank W. and Purtscheller F. (1999) Post-collisional potassio and ultrapotassic magmatism in SW Tibet: geochemical and Sr–Nd–Pb–O isotopic constraints for mantle source characteristics and petrogenesis. *J. Petrol.* **40**, 1399–1424.
- Mitsuishi M., Wallis S. R., Aoya M., Lee J. and Wang Y. (2012) E–W extension at 19 Ma in the Kung Co area, S. Tibet: Evidence for contemporaneous E–W and N–S extension in the Himalayan orogen. *Earth Planet. Sci. Lett.* **325–326**, 10–20.
- Mo X., Hou Z., Niu Y., Dong G., Qu X., Zhao Z. and Yang Z. (2007) Mantle contributions to crustal thickening during continental collision: evidence from Cenozoic igneous rocks in southern Tibet. *Lithos* **96**, 225–242.
- Mo X. X., Niu Y., Dong G., Zhao Z., Hou Z., Zhou S. and Ke S. (2008) Contribution of syncollisional felsic magmatism to continental crust growth: a case study of the Paleogene Linzizong volcanic succession in southern Tibet. *Chem. Geol.* **250**, 49–67.
- Molnar P. and Stock J. M. (2009) Slowing of India's convergence with Eurasia since 20 Ma and its implications for Tibetan mantle dynamics. *Tectonics* **28**. <http://dx.doi.org/10.1029/2008TC002271> (TC3001).
- Moyen J. F. (2009) High Sr/Y and La/Yb ratios: the meaning of the “adakitic signature”. *Lithos* **112**, 556–574.
- Müller D., Rock N. M. S. and Groves D. I. (1992) Geochemical discrimination between shoshonitic and potassio volcanic rocks in different tectonic settings: a pilot study. *Miner. Petrol.* **46**, 259–289.
- Nábělek J., Hetényi G., Vergne J., Sapkota S., Kafle B., Jiang M., Su H., Chen J. and Huang B. S. (2009) Underplating in the Himalaya–Tibet collision zone revealed by the Hi-CLIMB experiment. *Science* **325**, 1371–1374.
- Niu X. L., Zhao Z. D., Mo X. X., DePaolo D. J., Dong G. C., Zhang S. Q., Zhu D. C. and Guo T. Y. (2006) Elemental and Sr–Nd–Pb isotopic geochemistry for basic rocks from Decun–Angren ophiolites in Xigaze area, Tibet: implications for the characteristics of the Tethyan upper mantle domain. *Acta Petrol. Sin.* **22**, 2875–2888.
- Niu Y. L., Zhao Z. D., Zhu D. C. and Mo X. X. (2013) Continental collision zones are primary sites for net continental crust growth – a testable hypothesis. *Earth Sci. Rev.* **127**, 96–110.
- Nomade S., Renne P. R., Mo X., Zhao Z. and Zhou S. (2004) Miocene volcanism in the Lhasa block, Tibet: spatial trends and geodynamic implications. *Earth Planet. Sci. Lett.* **221**, 227–243.
- Owens T. J. and Zandt G. (1997) Implications of crustal property variations for models of Tibetan plateau evolution. *Nature* **387**, 37–43.
- Pertermann M. and Hirschmann M. M. (2002) Trace-element partitioning between vacancy-rich eclogitic clinopyroxene and silicate melt. *Am. Mineral.* **87**, 1365–1376.
- Pertermann M., Hirschmann M. M., Hametner K., Günther D. and Schmidt M. W. (2004) Experimental determination of trace element partitioning between garnet and silica-rich liquid during anhydrous partial melting of MORB-like eclogite. *Geochim. Geophys. Geosyst.* **5**. <http://dx.doi.org/10.1029/2003GC000638> (Q05A01).
- Pilet S., Baker M. B., Müntener O. and Stolper E. M. (2011) Monte Carlo simulations of metasomatic enrichment in the lithosphere and implications for the source of alkaline basalts. *J. Petrol.* **52**, 1415–1442.
- Plank T. and Langmuir C. H. (1998) The chemical composition of subducting sediment and its consequences for the crust and mantle. *Chem. Geol.* **145**, 325–394.
- Prelević D., Akal C., Foley S. F., Romer R. L., Stracke A. and Van Den Bogaard P. (2012) Ultrapotassic mafic rocks as geochemical proxies for post-collisional dynamics of orogenic lithospheric mantle: the case of Southwestern Anatolia, Turkey. *J. Petrol.* **53**, 1019–1055.

- Richards J. P. and Kerrich R. (2007) Special paper: adakite-like rocks: their diverse origins and questionable role in metallogenesis. *Econ. Geol.* **102**, 537–576.
- Royden L. H., Burchfiel B. C. and van der Hilst R. D. (2008) The geological evolution of the Tibetan Plateau. *Science* **321**, 1054–1058.
- Rubatto D. (2002) Zircon trace element geochemistry: partitioning with garnet and the link between U–Pb ages and metamorphism. *Chem. Geol.* **184**, 123–138.
- Rudnick R. L. and Gao S. (2003). Composition of the continental crust. In *The Crust* (ed. R. L. Rudnick), vol. 3 *Treatise on Geochemistry* (eds. H. D. Holland and K. K. Turekian). Elsevier-Pergamon, Oxford. pp. 1–64.
- Sobolev A. V., Hofmann A. W., Sobolev S. V. and Nikogosian I. K. (2005) An olivine-free mantle source of Hawaiian shield basalts. *Nature* **434**, 590–597.
- Spandler C., Yaxley G., Green D. H. and Rosenthal A. (2008) Phase relations and melting of anhydrous K-bearing eclogite from 1200 to 1600 °C and 3 to 5 GPa. *J. Petrol.* **49**, 771–795.
- Spicer R. A., Harris N. B. W., Widdowson M., Herman A. B., Guo S., Valdes P. J., Wolfe J. A. and Kelley S. P. (2003) Constant elevation of southern Tibet over the past 15 million years. *Nature* **421**, 622–624.
- Sun C. G., Zhao Z. D., Mo X. X., Zhu D. C., Dong G. C., Zhou S., Chen H. H., Xie L. W., Yang Y. H., Sun J. F. and Yu F. (2008) Enriched mantle source and petrogenesis of Sailipu ultrapotassic rocks in southwestern Tibet Plateau: constraints from zircon U–Pb geochronology and Hf isotopic compositions. *Acta Petrol. Sin.* **24**, 249–264.
- Sun C. and Liang Y. (2012) Distribution of REE between clinopyroxene and basaltic melt along a mantle adiabat: effects of major element composition, water, and temperature. *Contrib. Miner. Petrol.* **163**, 807–823.
- Sun S. S. and McDonough W. F. (1989) *Chemical and isotopic systematics of oceanic basalts: implications for mantle composition and processes*. Geological Society 42. Special Publications, London, 313–345.
- Tenner T. J., Hirschmann M. M. and Humayun M. (2012) The effect of H₂O on partial melting of garnet peridotite at 3.5 GPa. *Geochim. Geophys. Geosyst.* **13**. <http://dx.doi.org/10.1029/2011GC003942> (Q03016).
- Tomasini S., Avanzinelli R. and Conticelli S. (2010) The Th/La and Sm/La conundrum of the Tethyan realm lamproites. *Earth Planet. Sci. Lett.* **301**, 469–478.
- Turner S., Arnaud N., Liu J., Rogers N., Hawkesworth C., Harris N., Kelley S., Van Calsteren P. and Deng W. (1996) Post-collision, shoshonitic volcanism on the Tibetan Plateau: implications for convective thinning of the lithosphere and the source of ocean island basalts. *J. Petrol.* **37**, 45–71.
- Uddin A. and Lundberg N. (2004) Miocene sedimentation and subsidence during continent–continent collision, Bengal basin, Bangladesh. *Sediment. Geol.* **164**, 131–146.
- Valley J. W., Lackey J. S., Cavosie A. J., Clechenko C. C., Spicuzza M. J., Basei M. A. S., Bindeman I. N., Ferreira V. P., Sial A. N. and King E. M. (2005) 4.4 billion years of crustal maturation: oxygen isotope ratios of magmatic zircon. *Contrib. Miner. Petrol.* **150**, 561–580.
- van Hinsbergen D. J. J., Steinberger B., Doubrovine P. V. and Gassmöller R. (2011) Acceleration and deceleration of India–Asia convergence since the Cretaceous: roles of mantle plumes and continental collision. *J. Geophys. Res.* **116**. <http://dx.doi.org/10.1029/2010JB008051> (B06101).
- Vidal P., Cocherie A. and Le Fort P. (1982) Geochemical investigations of the origin of the Manaslu leucogranite (Himalaya, Nepal). *Geochim. Cosmochim. Acta* **46**, 2279–2292.
- Wang C., Jin Z., Gao S., Zhang J. and Zheng S. (2010) Eclogite-melt/peridotite reaction: experimental constrains on the destruction mechanism of the North China Craton. *Sci. China Earth Sci.* **53**, 797–809. <http://dx.doi.org/10.1007/s11430-010-3084-2>.
- Weyer S., Münker C. and Mezger K. (2003) Nb/Ta, Zr/Hf and REE in the depleted mantle: implications for the differentiation history of the crust–mantle system. *Earth Planet. Sci. Lett.* **205**, 309–324.
- Wiedenbeck M., Alle P., Corfu F., Griffin W. L., Meier M., Oberli F., Quadtt A., Roddick J. C. and Spiegel W. (1995) Three natural zircon standards for U–Th–Pb, Lu–Hf, trace element and REE analyses. *Geostand. Geoanal. Res.* **19**, 1–23.
- Williams H., Turner S., Kelley S. and Harris N. (2001) Age and composition of dikes in southern Tibet: New constraints on the timing of east–west extension and its relationship to postcollisional volcanism. *Geology* **29**, 339–342.
- Williams H. M., Turner S. P., Pearce J. A., Kelley S. P. and Harris N. B. W. (2004) Nature of the source regions for post-collisional, potassiac magmatism in southern and northern Tibet from geochemical variations and inverse trace element modeling. *J. Petrol.* **45**, 555–607.
- Woodhead J. D., Hergt J. M., Davidson J. P. and Eggin S. M. (2001) Hafnium isotope evidence for ‘conservative’ element mobility during subduction zone processes. *Earth Planet. Sci. Lett.* **192**, 331–346.
- Woodhead J., Hergt J., Shelley M., Eggin S. and Kemp R. (2004) Zircon Hf-isotope analysis with an excimer laser, depth profiling, ablation of complex geometries, and concomitant age estimation. *Chem. Geol.* **209**, 121–135.
- Wu F. Y., Ji W. Q., Liu C. Z. and Chung S. L. (2010) Detrital zircon U–Pb and Hf isotopic data from the Xigaze fore-arc basin: Constraints on Transhimalayan magmatic evolution in southern Tibet. *Chem. Geol.* **271**, 13–25.
- Xu J. F. and Castillo P. R. (2004) Geochemical and Nd–Pb isotopic characteristics of the Tethyan asthenosphere: implications for the origin of the Indian Ocean mantle domain. *Tectonophysics* **393**, 9–27.
- Yin A. and Harrison T. M. (2000) Geologic evolution of the Himalayan–Tibetan orogen. *Annu. Rev. Earth Planet. Sci.* **28**, 211–280.
- Yuan H. L., Gao S., Dai M. N., Zong C. L., Günther D., Fontaine G. H., Liu X. M. and Diwu C. R. (2008) Simultaneous determinations of U–Pb age, Hf isotopes and trace element compositions of zircon by excimer laser-ablation quadrupole and multiple-collector ICP-MS. *Chem. Geol.* **247**, 100–118.
- Zeng L., Gao L. E., Xie K. and Jing L. Z. (2011) Mid-Eocene high Sr/Y granites in the Northern Himalayan Gneiss Domes: melting thickened lower continental crust. *Earth Planet. Sci. Lett.* **303**, 251–266.
- Zhang S. Q., Mahoney J. J., Mo X. X., Ghazi A. M., Milani L., Crawford A. J., Guo T. Y. and Zhao Z. D. (2005) Evidence for a widespread Tethyan upper mantle with Indian-Ocean-type isotopic characteristics. *J. Petrol.* **46**, 829–858.
- Zhang Z., Dong X., Santosh M., Liu F., Wang W., Yiu F., He Z. and Shen K. (2012) Petrology and geochronology of the Namche Barwa complex in the eastern Himalayan syntaxis, Tibet: constraints on the origin and evolution of the north-eastern margin of the Indian Craton. *Gondwana Res.* **23**, 123–137.
- Zhao Z., Mo X., Zhang S., Guo T., Zhou S., Dong G. C. and Wang Y. (2001) Post-collisional magmatism in Wuyu basin, central Tibet: evidence for recycling of subducted Tethyan oceanic crust. *Sci. China D* **44**, 27–34.
- Zhao Z., Mo X. X., Nomade S., Renne P. R., Zhou S., Dong G. C., Wang L. L., Zhu D. C. and Liao Z. L. (2006) Post-collisional

- ultrapotassic rocks in Lhasa block: spatial and temporal distributions and its implications. *Acta Petrol. Sin.* **22**, 787–794.
- Zhao Z., Mo X. X., Dong G. C., Zhou S., Zhu D. C., Wang L. L., Liao Z. L. and Sun C. G. (2007) Pb isotopic geochemistry of Tibetan Plateau and its implications. *Geoscience* **21**, 265–274.
- Zhao Z., Mo X. X., Sun C. G., Zhu D. C., Niu Y. L., Dong G. C., Zhou S., Dong X. and Liu Y. S. (2008) Mantle xenoliths in southern Tibet: geochemistry and constraints for the nature of the mantle. *Acta Petrol. Sin.* **24**, 193–202.
- Zhao Z., Mo X., Dilek Y., Niu Y., DePaolo D. J., Robinson P., Zhu D., Sun C., Dong G. and Zhou S. (2009) Geochemical and Sr–Nd–Pb–O isotopic compositions of the post-collisional ultrapotassic magmatism in SW Tibet: petrogenesis and implications for India intra-continental subduction beneath southern Tibet. *Lithos* **113**, 190–212.
- Zhao Z., Zhu D. C., Dong G. C., Mo X. X., DePaolo D. J., Jia L., Hu Z. C. and Yuan H. L. (2011) The ~54 Ma gabbro–granite intrusive in southern Dangxung area, Tibet: petrogenesis and implications. *Acta Petrol. Sin.* **27**, 3513–3524.
- Zhu D. C., Zhao Z. D., Niu Y., Mo X. X., Chung S. L., Hou Z. Q., Wang L. Q. and Wu F. Y. (2011a) The Lhasa terrane: record of a microcontinent and its histories of drift and growth. *Earth Planet. Sci. Lett.* **301**, 241–255.
- Zhu D. C., Zhao Z. D., Niu Y., Dilek Y. and Mo X. X. (2011b) Lhasa terrane in southern Tibet came from Australia. *Geology* **39**, 727–730.
- Zhu D. C., Zhao Z. D., Niu Y., Dilek Y., Wang Q., Ji W. H., Dong G. C., Sui Q. L., Liu Y. S., Yuan H. L. and Mo X. X. (2012a) Cambrian bimodal volcanism in the Lhasa Terrane, southern Tibet: record of an early paleozoic Andean-type magmatic arc in the Australian proto-Tethyan margin. *Chem. Geol.* **328**, 290–308.
- Zhu D. C., Zhao Z. D., Niu Y., Dilek Y., Wang Q. and Mo X. X. (2012b) Temporal changes in magma geochemistry in the northern Lhasa Terrane, Tibet: response to the Lhasa–Qiangtang collision. Goldschmidt (abstr.).
- Zhu D. C., Zhao Z. D., Niu Y., Dilek Y., Hou Z. Q. and Mo X. X. (2013) Origin and pre-Cenozoic evolution of the Tibetan Plateau. *Gondwana Res.* **23**, 1429–1454.
- Zindler A. and Hart S. (1986) Chemical geodynamics. *Annu. Rev. Earth Planet. Sci.* **14**, 493–571.

Associate editor: Weidong Sun